

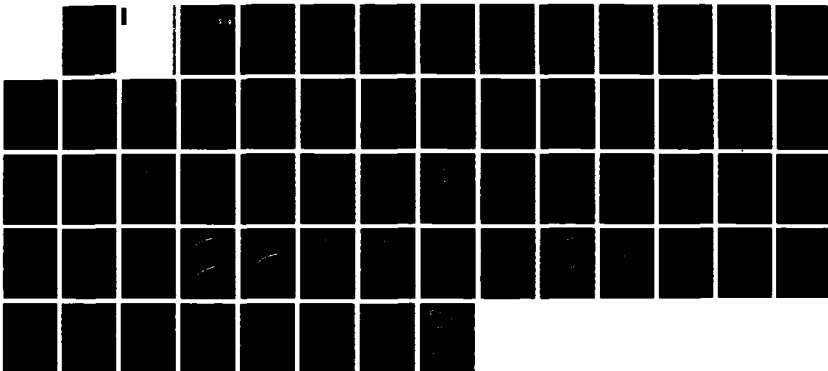
NO-A190 120

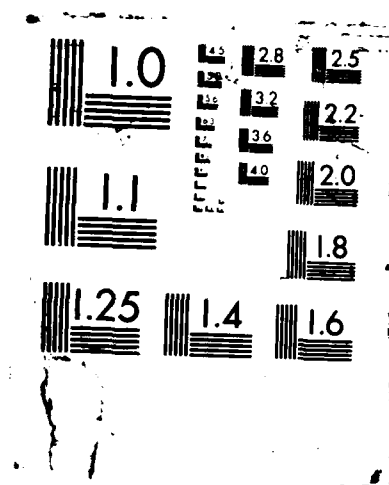
UNSTEADY AERODYNAMICS OF A NORTHMAN FX-63-117 WING IN A 1/1  
FLUCTUATING WIND FIELD(U) FLOW RESEARCH CO KENT WA  
H LIU NOV 87 FLOW-RR-431 N00014-83-C-0694

UNCLASSIFIED

F/G 1/1

NL





(4)

# REPORT DOCUMENTATION PAGE

1a. REPORT SECURITY CLASSIFICATION Unclassified			1b. RESTRICTIVE MARKINGS		
2a. SECURITY CLASSIFICATION AUTHORITY			3. DISTRIBUTION/AVAILABILITY OF REPORT Approved for Public Release; Distribution Unlimited		
2b. DECLASSIFICATION/DOWNGRADING SCHEDULE					
4. PERFORMING ORGANIZATION REPORT NUMBER(S) Flow Research Report No. 431			5. MONITORING ORGANIZATION REPORT NUMBER(S)		
6a. NAME OF PERFORMING ORGANIZATION Flow Research, Inc.		6b. OFFICE SYMBOL (if applicable)	7a. NAME OF MONITORING ORGANIZATION DTIC ELECTE JAN 13 1988 S D		
6c. ADDRESS (City, State, and ZIP Code) 21414 - 68th Avenue South Kent, WA 98032			7b. ADDRESS (City, State, and ZIP Code)		
8a. NAME OF FUNDING/SPONSORING ORGANIZATION Office of Naval Research		8b. OFFICE SYMBOL (if applicable) N00014	9. PROCUREMENT INSTRUMENT IDENTIFICATION NUMBER N00014 - 83 - C - 0694		
8c. ADDRESS (City, State, and ZIP Code) 800 North Quincy Street Arlington, VA 22217			10. SOURCE OF FUNDING NUMBERS		
			PROGRAM ELEMENT NO.	PROJECT NO.	TASK NO.
			WORK UNIT ACCESSION NO.		
11. TITLE (Include Security Classification) Unsteady Aerodynamics of a Wortmann FX-63-137 Wing in a Fluctuating Wind Field					
12. PERSONAL AUTHOR(S) H.-T. Liu					
13a. TYPE OF REPORT Final		13b. TIME COVERED FROM 9-15-83 TO 9-15-87		14. DATE OF REPORT (Year, Month, Day) November 1987	
15. PAGE COUNT 54					
16. SUPPLEMENTARY NOTATION					
17. COSATI CODES			18. SUBJECT TERMS (Continue on reverse if necessary and identify by block number)		
FIELD	GROUP	SUB-GROUP	Dynamic Stall, Hysteresis, Aerodynamic Damping, Stall Flutter		
			Low Reynolds Number, Unsteady Aerodynamics, Lift, Drag,		
			Pitching Moment, Endurance, Atmosphere Boundary Layer, (Cont.)		
19. ABSTRACT (Continue on reverse if necessary and identify by block number)  An environmental aerodynamic test system (EATS) was designed and assembled to investigate the effects of gust and turbulence on the performance of a full-scale Wortmann FX-63-137 wing. Experiments were conducted in the atmospheric boundary layer by directing the elevated wing into the prevailing wind for a range of Reynolds numbers from 80,000 to 450,000. The unsteady wind field, in essence, introduces significant and favorable effects on the aerodynamics in terms of lift overshoot, stall delay, reduction of drag at small angles of attack, and endurance enhancement. Further analysis of the field data was conducted to investigate the unsteady aerodynamic phenomena, such as the hysteresis loops and the spectra of the aerodynamic forces and their relation to the ambient wind conditions. One of the important findings is that the spectral characteristics of the wind field when normalized by the turbulence intensity satisfies a similarity relation. This similarity					
20. DISTRIBUTION/AVAILABILITY OF ABSTRACT <input checked="" type="checkbox"/> UNCLASSIFIED/UNLIMITED <input type="checkbox"/> SAME AS RPT. <input type="checkbox"/> DTIC USERS			21. ABSTRACT SECURITY CLASSIFICATION Unclassified		
22a. NAME OF RESPONSIBLE INDIVIDUAL Robert E. Whitehead			22b. TELEPHONE (Include Area Code) (206) 696-4404		22c. OFFICE SYMBOL N00014

18. (Continued) Wind Speed, Turbulence, Reduced Frequency.

19. (Continued)

relation effectively removes the dependence of the unsteady phenomena on the wind speed and thus provides a common basis for assessing the unsteady aerodynamics. For small angles of attack,  $\alpha$ , where  $C_L$  increases linearly with  $\alpha$  and  $C_M$  is roughly a constant, negative values of the drag, i.e., propulsion, are momentarily generated by the unsteady wind field, although the corresponding time-averaged values are positive. During a random cycle with a large-amplitude fluctuation in the instantaneous angle of attack, the wing may go through the entire dynamic stall regime. In the part of the cycle with  $\alpha$  increasing from its minimum value, the instantaneous  $C_L$  increases and greatly exceeds the maximum steady-state value before the onset of stall. The instantaneous stall angle also greatly exceeds the time-averaged dynamic stall angle. Meanwhile,  $C_D$  rises sharply as both induced and form drag increase. These lead to an abrupt drop in  $C_M$ . At stall onset,  $C_L$  levels off and drops slightly;  $C_M$  shows the same behavior except for a reversed sign; and  $C_D$  continues to rise because of the increase in form drag. Further increase in  $\alpha$  causes the wing to enter the light stall and finally the deep stall regimes.  $C_L$  drops slowly at first and then at an abrupt rate at deep stall. With further increase in  $\alpha$ ,  $C_L$  remains at a nearly constant value below its maximum static value.  $C_D$  drops and  $C_M$  rises sharply as  $C_L$  drops abruptly. However, the form drag continues to rise with increasing  $\alpha$  even when  $C_L$  ceases to decrease further. The force coefficients are restored to roughly their initial values as  $\alpha$  returns to a minimum at the end of the cycle. From the spectra of the aerodynamic parameters, the unsteady wind field has the maximum impact on the drag, with fewer but significant effects on the pitching moment and the lift. During dynamic stall, particularly at deep stall, the spectral densities increase significantly at high frequencies, and distinct spikes with well-defined dominant frequencies appear. These spikes strongly indicate the presence of the hysteresis loops.

# TABLE OF CONTENTS

	<u>Page</u>
REPORT DOCUMENTATION PAGE	i
LIST OF FIGURES	iv
ACKNOWLEDGMENTS	
1. INTRODUCTION	1
2. ENVIRONMENTAL AERODYNAMIC TEST SYSTEM (EAST)	7
3. RESULTS AND DISCUSSION	10
Time Series of Ambient and Aerodynamic Parameters	10
Hysteresis Loops of Aerodynamic Coefficients	28
Frequency Spectra of Ambient and Aerodynamic Parameters	36
4. SUMMARY	50
REFERENCES	53

Accession For	
NTIS CPA&I	<input checked="" type="checkbox"/>
DTIC TAB	<input type="checkbox"/>
Unannounced	<input type="checkbox"/>
Justification	
By	
Date	
Number of Pages	
Dist	Availability
A-1	



# LIST OF FIGURES

	<u>Page</u>
Figure 1. Effect of Mean Angle on Lift Moment Coefficients and on Aerodynamic Damping (from Reference 15; see also Reference 10).	5
Figure 2. Time Series of Wind Components (0.1-s averages) Measured at the Ellensburg Airport. $\bar{\alpha} = 3.4^\circ$ , $R_C = 318,000$ .	11
Figure 3. Time Series of Angles of Attack (0.1-s averages). $\bar{\alpha} = 3.4^\circ$ , $R_C = 318,000$ .	12
Figure 4. Time Series of Lift, Drag and Pitching Moment (0.1-s averages). $\bar{\alpha} = 3.4^\circ$ , $R_C = 318,000$ .	13
Figure 5. Time Series of Wind Components (0.1-s averages) Measured at the Ellensburg Airport. $\bar{\alpha} = 19.9^\circ$ , $R_C = 420,900$ .	17
Figure 6. Time Series of Angles of Attack (0.1-s averages). $\bar{\alpha} = 19.9^\circ$ , $R_C = 420,900$ .	18
Figure 7. Time Series of Lift, Drag and Pitching Moment (0.1-s averages). $\bar{\alpha} = 19.9^\circ$ , $R_C = 420,900$ .	19
Figure 8. Time Series of Wind Components (0.1-s averages) Measured at the Ellensburg Airport. $\bar{\alpha} = 23.0^\circ$ , $R_C = 360,000$ .	21
Figure 9. Time Series of Angles of Attack (0.1-s averages). $\bar{\alpha} = 23.0^\circ$ , $R_C = 360,000$ .	22
Figure 10. Time Series of Lift, Drag and Pitching Moment (0.1-s averages). $\bar{\alpha} = 23.0^\circ$ , $R_C = 360,000$ .	23
Figure 11. Time Series of Wind Components (0.1-s averages) Measured at the Ellensburg Airport. $\bar{\alpha} = 29.3^\circ$ , $R_C = 331,000$ .	25
Figure 12. Time Series of Angles of Attack (0.1-s averages). $\bar{\alpha} = 29.3^\circ$ , $R_C = 331,000$ .	26
Figure 13. Time Series of Lift, Drag and Pitching Moment (0.1-s averages). $\bar{\alpha} = 29.3^\circ$ , $R_C = 331,000$ .	27
Figure 14. Hysteresis Loops of $C_L$ for $\bar{\alpha} = 3.4^\circ$ , $19.9^\circ$ and $29.3^\circ$ . Series I.	29
Figure 15. Hysteresis Loops of $C_D$ for $\bar{\alpha} = 3.4^\circ$ , $19.9^\circ$ and $29.3^\circ$ . Series I.	29
Figure 16. Hysteresis Loops of $C_M$ for $\bar{\alpha} = 3.4^\circ$ , $19.9^\circ$ and $29.3^\circ$ . Series I.	30
Figure 17. Hysteresis Loops of $C_L$ for $\bar{\alpha} = 3.4^\circ$ , $19.9^\circ$ and $29.3^\circ$ . Series II.	30

# LIST OF FIGURES (CONT.)

	<u>Page</u>
Figure 18. Hysteresis Loops of $C_D$ for $\bar{\alpha} = 3.4^\circ, 19.9^\circ$ and $29.3^\circ$ . Series II.	31
Figure 19. Hysteresis Loops of $C_M$ for $\bar{\alpha} = 3.4^\circ, 19.9^\circ$ and $29.3^\circ$ . Series II.	31
Figure 20. Hysteresis Loops of $C_L$ for $\bar{\alpha} = 3.4^\circ, 19.9^\circ$ and $29.3^\circ$ . Series III.	32
Figure 21. Hysteresis Loops of $C_D$ for $\bar{\alpha} = 3.4^\circ, 19.9^\circ$ and $29.3^\circ$ . Series III.	32
Figure 22. Hysteresis Loops of $C_M$ for $\bar{\alpha} = 3.4^\circ, 19.9^\circ$ and $29.3^\circ$ . Series III.	33
Figure 23. Spectra of the U Component for Four Selected Runs.	37
Figure 24. Spectra of the W Component for Four Selected Runs.	37
Figure 25. Spectra of the Angle of Attack for Four Selected Runs.	38
Figure 26. Spectra of the Lift for Four Flow Regimes: No Stall, Stall Onset, Light Stall, and Deep Dynamic Stall.	39
Figure 27. Spectra of the Drag for Four Flow Regimes: No Stall, Stall Onset, Light Stall, and Deep Dynamic Stall.	40
Figure 28. Spectra of the Pitching Moment for Four Flow Regimes: No Stall, Stall Onset, Light Stall, and Deep Dynamic Stall.	41
Figure 29. Corrected Spectra of the U Component for Four Selected Runs.	43
Figure 30. Corrected Spectra of the W Component for Four Selected Runs.	43
Figure 31. Corrected Spectra of the Angle of Attack for Four Selected Runs.	44
Figure 32. Corrected Spectra of the Lift for Four Flow Regimes: No Stall, Stall Onset, Light Stall, and Deep Dynamic Stall.	45
Figure 33. Corrected Spectra of the Drag for Four Flow Regimes: No Stall, Stall Onset, Light Stall, and Deep Dynamic Stall.	46
Figure 34. Corrected Spectra of the Pitching Moment for Four Flow Regimes: No Stall, Stall Onset, Light Stall, and Deep Dynamic Stall.	47

## ACKNOWLEDGMENTS

The author would like to thank Dr. W.-H. Jou for reviewing this report. Both Dr. Jou and Mr. E. W. Geller have provided invaluable suggestions throughout the course of the investigation.



## 1. INTRODUCTION

On 7 February 1983, the Office of Naval Research (ONR) convened a Workshop on Low-Reynolds-Number Aerodynamics (in the Reynolds number range from 200,000 to 1,000,000) to review and appraise the status of aerodynamic data and theory for the design of low-speed, low-altitude remotely piloted vehicles (RPVs).<sup>1</sup> Such RPVs are potentially to be deployed as decoys of a naval fleet, confusing the enemy's radar system so that the positions of the fleet cannot be accurately detected. A special focus program was subsequently established at ONR to investigate low-Reynolds-number and low-altitude aerodynamics. The present report presents our effort in investigating the effects of atmospheric unsteadiness on the performance of a full-scale Wortmann FX-63-137 wing.

The status of the knowledge of aerodynamics for low-speed, low-altitude decoys can be reviewed conveniently from several technical viewpoints: an unperturbed versus a real atmosphere; two- versus three-dimensional flows; and lift coefficients less than approximately 1.5 to 1.7 versus higher lift coefficients. To date, essentially all the research data have been obtained in what was hoped to be an unperturbed flow. Unfortunately, the data are contaminated to some degree by disturbances inherent in the test procedure (wind tunnel or flight). Based on the most reliable data,<sup>1,2</sup> at least for the higher Reynolds number flows, lift coefficients up to roughly 1.5 to 1.7 are obtainable for two-dimensional airfoils ("unperturbed atmosphere") designed for high lift that have been experimentally verified for a limited number of cases.

For the lower range of Reynolds numbers of interest, to quote Lissaman,<sup>3</sup> ". . .the design of low-Reynolds-number airfoils, particularly at Reynolds numbers below 300,000, is still a black art" (also see Mueller<sup>4</sup>). A qualitative picture of the flow around an airfoil with lift coefficients in this range, under steady conditions, is available. Detailed quantitative information on the upper surface bubble structure, its role in the transition process, and the transition process itself is not available, especially for an unsteady environment such as the lower atmospheric boundary layer over the ocean surface. Although there is a dearth of detailed pressure data for the three-dimensional wings, Lieback has commented that rather simplified design procedures have met with reasonable success in predicting the gross aerodynamic characteristics of three-dimensional wings.<sup>1,5</sup>

A lift coefficient in the range of 1.5 to 1.7 is quite low for even approaching a down-graded compromise in the RPV requirements.<sup>1</sup> It appears that

any attempts to obtain significantly higher lift coefficients will require more exotic airfoils (fixed multi-element airfoils, movable multi-element airfoils<sup>6</sup> or blowing). A compromise among the design criteria is clearly required when such added complexity is incorporated into the design of future RPVs. In any case, the development of such higher lift airfoils would benefit by a better understanding of the flow—an understanding that can be achieved only through extensive experimentation. An extensive experimental program is beyond the scope of the present work. Instead, the present experiments are dedicated to investigating one of the major uncertainties of the performance of low-Reynolds-number wings, i.e., the effects of atmospheric unsteadiness. While such effects are known to be significant in many instances,<sup>1,7</sup> no method of quantification exists. Even if the atmospheric turbulence and related parameters were known in detail (though according to Spence<sup>1</sup> they certainly are not available), their impact on the aerodynamic performance of a wing under such conditions could be estimated only in the crudest fashion.

For a low-speed and low-altitude decoy RPV, the gust and turbulence in the atmospheric boundary layer are expected to have significant effects on its performance. One of these effects is due to the unsteadiness of the wind field, which effectively causes the wing of the RPV to experience unsteady pitching/plunging motions when the reference frame is fixed on the wing. In particular, under the influence of the low-frequency fluctuating wind components, the wing is predominantly subject to an unsteady plunging rather than pitching motion relative to the instantaneous wind field. When an airfoil undergoes oscillatory motions, i.e., pitching or plunging, several dramatic phenomena that deviate greatly from the static situation take place. A brief review of the unsteady aerodynamics is given below. For more detailed information relevant to the present investigation, the readers are referred to Liu.<sup>8</sup>

When the angle of attack oscillates around a mean value  $\alpha_0$  near or greater than the static stall angle, the maximum values of lift, drag, and pitching moment ( $C_L$ ,  $C_D$ , and  $|C_M|$ , respectively) can greatly exceed their static counterparts. The higher value in the lift coefficient is generally referred to as the "lift overshoot." Such increases in  $C_L$ ,  $C_D$ , and  $|C_M|$  cannot be reproduced even qualitatively by neglecting the unsteady motion of the airfoil. During the oscillatory cycles, large hysteresis develops in the aerodynamic forces and moments with respect to the instantaneous angle. The above process is referred to as dynamic stall, which is intimately related to unsteady

separation of the flow from the oscillating airfoil. The process of dynamic stall may be classified into three important regimes, namely, stall onset, light stall and deep stall, depending on the state of the viscous-inviscid interaction for an oscillating airfoil.<sup>9,10</sup> Stall onset is the limiting case of the maximum unsteady lift that can be obtained with no significant penalty in pitching moment and drag. Further increase in  $\alpha$  beyond  $\alpha_{max}$  results in dynamic stall, which is characterized by large phase lags and hysteresis in the separation and reattachment of the viscous flow. In the light stall regime, the scale of the flow separation remains on the order of the airfoil thickness. As the maximum incidence increases to values well beyond the static stall angle, the flow over the airfoil is in the deep stall regime. A strong vortex-like disturbance initiates in the leading edge region and subsequently sheds from the airfoil and moves downstream over the upper surface of the airfoil. The process produces large-amplitude hysteresis in  $C_L$ ,  $C_D$ , and  $C_M$ . The scale of the viscous interaction zone is on the order of the airfoil chord.

For an airfoil undergoing a periodic plunging motion, a similar response in the deep stall regime has been shown,<sup>11</sup> but significantly different responses in the light stall regime have been reported.<sup>12,13</sup> In essence, the stall cell is not well organized and, when it occurs, it has no orderly downstream propagation. The vortex-like disturbance moves downstream over the airfoil surface at a relatively slow speed. The vortex does not have a strong peak, and the low-pressure zone formed on the upper surface is elongated. As a result, a high lift coefficient could be sustained for a relatively long period of time when the angle of attack increases beyond the static stall angle.<sup>11</sup>

The studies of Maresca et al.<sup>11</sup> also established the existence of vortex-shedding phenomena and strong hysteresis effects due to translational oscillations in the streamwise direction and at various oblique angles relative to the oncoming flow. Unsteady effects were found to be strong enough to prevent stalling during part of the cycle. St. Hilaire et al.<sup>14</sup> examined the effects of wing sweep at an angle  $\lambda$  with respect to the free stream for an oscillating wing. Their results show that the wing sweep tends to delay the onset of dynamic stall and to reduce the rate of change of  $C_L$  and  $C_M$  as the stall begins. It also reduces somewhat the amplitude of the hysteresis loops.

Another unsteady phenomenon of great concern pertains to the aerodynamic damping. For a wing undergoing unsteady oscillation, the instantaneous work done on the fluid by the wing due to its motion is  $dW = -M d\alpha$ , where  $M$  is the

pitching moment about the axis of the rotation and is positive for nose-up airloads. Normally,  $C_M d\alpha$  is negative, but it can become positive during some phase of dynamic stall.<sup>10</sup> As a result, work is being done on the wing by the fluid. A pitching-damping parameter, defined as  $\zeta = \int C_M d\alpha / 4\alpha$ , is a measure of the net work done over a complete cycle of unsteady motion. If  $\zeta$  is negative, the wing extracts energy from the airstream, and the unsteady motion may increase in amplitude unless restrained. This, of course, is the condition of flutter. Stall flutter, arising from this negative pitch damping, tends to occur when the airfoil is oscillating in and out of stall. The phenomenon of stall flutter is illustrated in Figure 1.<sup>15,10</sup> As shown in the figure,  $\zeta$  is positive throughout the cycle when  $\alpha_0 = 7.3^\circ$  (not stalled) and when  $\alpha_0 = 24.6^\circ$  (remain stalled). For  $\alpha_0 = 14.9^\circ$ , however, the airfoil is stalled part of the time and not at all at other times, and the areas inside the clockwise loop ( $\zeta < 0$ ) and counterclockwise loops ( $\zeta > 0$ ) are approximately the same, indicating neutral stability. Had the mean angle been slightly less, the net damping would probably have been negative, and the oscillation would therefore have been unstable if unconstrained. Stall flutter may also occur in plunging oscillation when the wing is in and out of stall under the influence of a relatively large-amplitude fluctuation of the vertical wind components, which may potentially exist near the ocean surface at high sea states. Stall flutter may lead to structural damage due to material fatigue provided the frequency of the stall flutter is in resonance with the natural frequency of the RPV wing.

To fill this serious gap in our knowledge of the environmental effects, Flow Research, Inc. (FLOW) has engaged in a unique experimental investigation to quantify such effects on the low-Reynolds-number aerodynamic characteristics of full-scale wings representative of an advanced RPV configuration. The main thrust of FLOW's involvement was to collect and analyze full-scale experimental data and to understand the behavior of the flow field around low-Reynolds-number (LRN) wings under various environmental conditions often encountered by RPVs during their operations. Up to the present, we have investigated the effects of atmospheric gust and turbulence. The efforts were divided into two phases. During Phase I, an environmental aerodynamic test system (EATS) was designed and built.<sup>16</sup> In Phase II, several series of experiments were conducted to investigate the effects of atmospheric unsteadiness on the performance of the Wortmann wing.<sup>8</sup> The results of full-scale testing were compared with the wind tunnel data obtained with the same wing under steady conditions.<sup>17,18</sup>

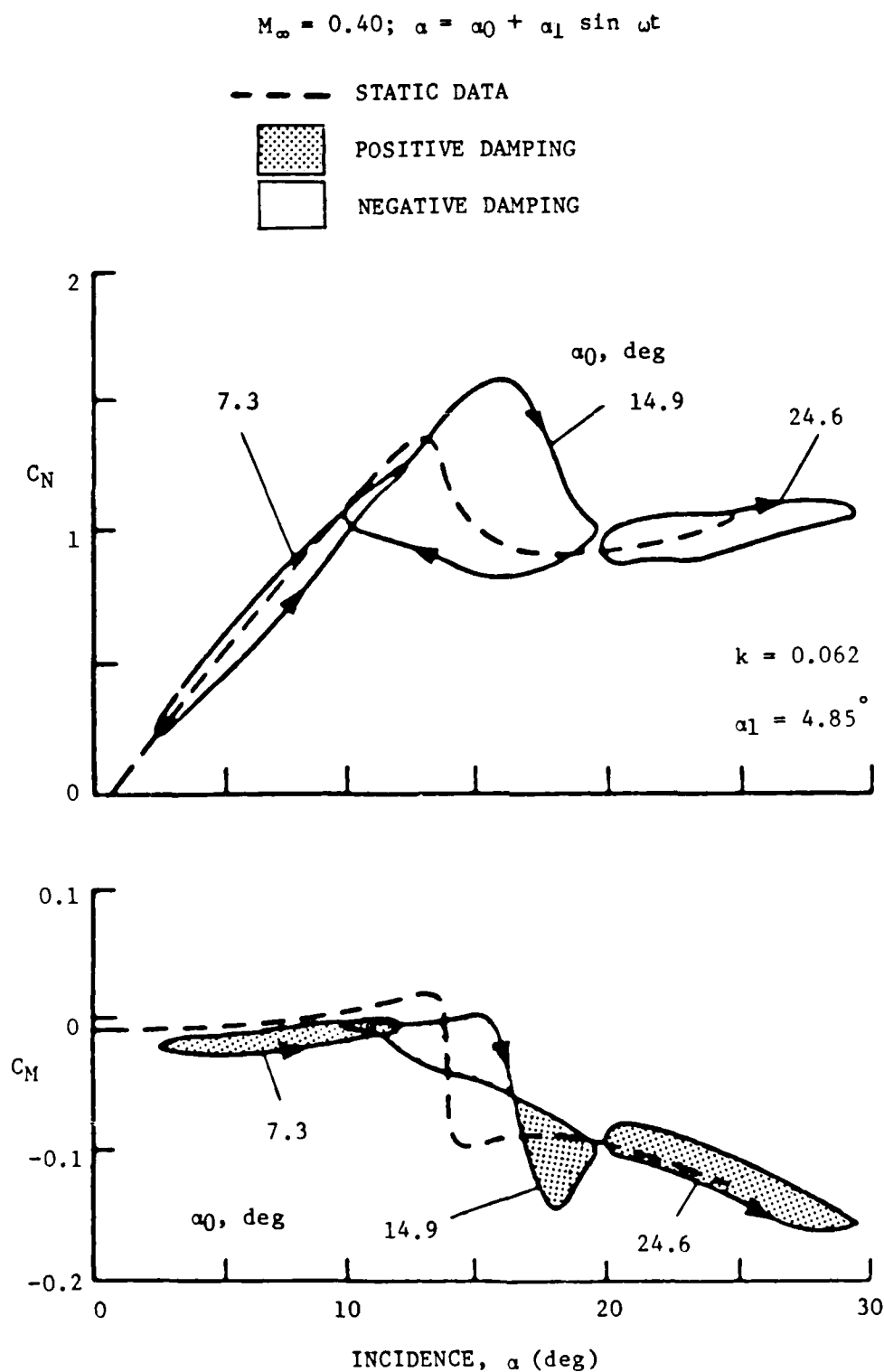


Figure 1. Effect of Mean Angle on Lift Moment Coefficients and on Aerodynamic Damping (from Reference 15; see also Reference 10).

The wind tunnel results serve as baseline cases for assessing the unsteady effects of the wind field on the performance of the Wortmann wing. Much of the experimental results and their interpretation and assessment have been reported elsewhere.<sup>8</sup>

In this report, we summarize the most recent work performed in the research project. Most of the work has been reported in two technical papers,<sup>8,16</sup> and frequent reference to these papers is made to avoid unnecessary duplication and to ensure continuity. In addition to the results reported in these papers, the analyses of the high-frequency characteristics of the wind components and force/moment are presented in this report to explore other potentially important effects due to the unsteady nature of the wind field. We present the time series, the hysteresis and the spectra of the ambient and aerodynamic parameters. In particular, we attempt to explore the dynamic stall phenomenon that might lead to stall flutter. Stall flutter must be considered in the design and fabrication of the wings of RPVs. If not controlled, this flutter may result in serious structural damage to the RPV, particularly when complex wing shapes, such as a multi-element wing, are used to increase aerodynamic performance at the expense of structural integrity.

## 2. ENVIRONMENTAL AERODYNAMIC TEST SYSTEM (EATS)

During Phase I, an environmental aerodynamic test system (EATS) was designed and assembled for testing full-scale wings under a broad range of atmospheric conditions, including gust and turbulence, cross winds, rain and possibly snow. In its present form, the EATS consists of a full-scale Wortmann FX-63-137 wing (smoothed by Eppler) with a span of 3.67 m and a chord of 0.61 m mounted on an instrumented moving platform, a one-ton Ford truck. The EATS is equipped with a three-component aerodynamic balance (lift, drag and pitching moment) mounted inside the wing body and on a boom about 6-m above the ground. In addition to the forces and moment, the EATS is capable of simultaneous measurements of the atmospheric parameters, such as the three wind velocity components, the barometric pressure and temperature. For a detailed description of the EATS and its operation, refer to References 8 and 16.

The EATS was developed based on the design of a similar system for testing hang gliders.<sup>19</sup> For example, the original design of the flexures used in the aerodynamic balance were essentially a scaled-down version of those used by Pregler et al.<sup>19</sup> Miniature load cells with superior performance characteristics (in terms of sensitivity and temperature drift) to those used by Pregler et al. were incorporated into the new balance. Extensive tests were conducted to determine the performance of the EATS. Based on the test results, modifications of a few components were made to improve the performance characteristics. In particular, the scaled-down flexures were found to be too weak to handle the load generated by the full-scale Wortmann wing. The flexures were sheared off repeatedly at the narrow necks during testing. Subsequently, the flexures were redesigned using beryllium copper with a thin straight section 2.54 cm long and 0.24 cm in diameter, instead of using high-strength tool steel with two short narrow necks. The improved flexures worked reliably without a single failure during all the experiments. Another modification was to add two flexures (without the load cells) to increase the stability in the yaw direction. But this resulted in a loss of the capability of providing the yaw measurement. To match the dynamic response of the balance and the wind sensors (Gill propeller anemometers with a dynamic response of 2 Hz at 8 m/s), 4- to 5-Hz low-pass filters were installed in the output circuitries of the forces and moment controller.

Two mini-clinometers (Sperry Corporation) were used to set and monitor the angle of attack and the leveling of the truck in the two horizontal planes.

Leveling of the EATS in the horizontal plane was achieved by jacking up the truck at three points under the main body frame, once the prevailing wind direction was determined. A third clinometer was used to monitor the inclination angle of the Gill anemometers.

During the initial tests, we discovered that the force/moment data were seriously contaminated by the vehicle vibration induced by road roughness when the EATS was operating in a run mode along a runway or an automobile racing track. Significant modifications to incorporate a sophisticated damping system would be required to remove the contamination. These modifications were not possible due to budgetary constraints. The run-mode approach was then discarded for the present investigation. To avoid vehicle-induced contamination, several series of experiments were conducted under a park-mode configuration by directing the wing into the prevailing wind.

The results were grouped into two series with Reynolds numbers in the range of 80,000 to 200,000 and 250,000 to 450,000. The first series (low  $R_c$ ) was conducted at the parking lot of FLOW during windy days. Depending on the wind direction, the upwind ground features were either a large vacant lot with low brush (facing south) or a long alley formed by several warehouse buildings (facing north). The wind field was quite unsteady with the wind speed and direction varying noticeably during the experiments. When the wind direction changed momentarily, vortices shed from the corners of buildings and tree tops were observed from a flow visualization experiment using smoke as the tracer. The reference runs were conducted downwind of a warehouse building. The results were carefully screened to discard those runs during which significant changes in the wind conditions took place.

The second series of experiments (high  $R_c$ ) was conducted at the Ellensburg Airport, Ellensburg, Washington, located east of Snoqualmie Pass in the Cascade Mountains. During the months of March through July, steady and strong seasonal winds up to 20 m/s are common through the pass. The upwind terrain is exceptionally flat for miles with very low desert plants. During the experiments, the wind conditions were relatively steady except for the turbulence generated by the flat terrain upwind. The reference runs were conducted in a hanger, which provided an ideal and quiescent environment. For each angle of attack, we conducted a series of about 10 runs. Reference runs were conducted before and/or after each series of runs. See Reference 8 for a description of the procedures for setting up the reference runs and for the force/moment measurements.



As reported by Liu,<sup>8</sup> the quality of the data obtained in the second series was significantly better than that of the first series. In particular, the data scatter is noticeably higher for the low-Reynolds-number series than for the high-Reynolds-number series, as expected.

### 3. RESULTS AND DISCUSSION

Most of the essential results were reported previously in the papers by Liu et al.<sup>16</sup> and Liu.<sup>8</sup> The first paper presented a detailed description of the EATS and some preliminary test results. The second paper discussed the latest modifications of the EATS and presented the results of the two series of full-scale experiments. Refer to these two papers for detailed information.

In this report, we present additional analyses that are oriented toward investigating the unsteady nature of the results. First, we present four sets of time series covering a range of mean angles of attack from small to beyond dynamic stall. Second, we examine the unsteady aerodynamics by selecting from the time series several individual cycles with large amplitudes. In particular, we illustrate the unsteady loops of  $C_L$ ,  $C_D$ , and  $C_M$  for three different cycles for angles well below the static stall angle (SSA), in the neighborhood of and well exceeding the time-averaged dynamic stall angle (DSA). We anticipated that the hysteresis loops would be different from those of an oscillating airfoil as derived from wind tunnel experiments.<sup>12,13</sup> Such information would shed light on the formation of the hysteresis in the three different flow regimes. Comparison will be made with laboratory results obtained by an oscillating airfoil in a steady air stream. Finally, we will present the frequency spectra of the wind components, forces and moment. The spectral decomposition of these quantities would provide additional information concerning the unsteady aerodynamics which lead to lift overshoot, dynamic stall and potentially to stall flutter.

#### Time Series of Ambient and Aerodynamic Parameters

Figures 2 through 4 show the time series of the three wind components,  $U$ ,  $V$ , and  $W$ , the lift, drag, pitching moment and angles of attack for one of the runs with  $\bar{\alpha} = 3.4^\circ$ . The  $W$  component is shifted by  $-6$  m/s to improve the readability of the figures. The Reynolds number and the turbulence intensity are  $R_c = 318,000$  and  $0.12$ , respectively. The averaged angle of attack  $\bar{\alpha}$  corresponds to the condition at the minimum drag ( $D = 3.65$  N and  $C_D = 0.025$ ) [see Table 1 and Reference 8]. In general, the lift, drag and pitching moment depend on both  $U$  and  $\alpha$ , whereas the force coefficients depend only on  $\alpha$  within a narrow range of  $R_c$ . At this small  $\alpha$ ,  $C_L$  increases linearly with  $\alpha$  while  $C_D$  has the minimum value. The lift and drag increase whereas the pitching moment decreases with increasing  $U$  and  $\alpha$ . From the figures, the lift and pitching

WRN4101/10 Hz

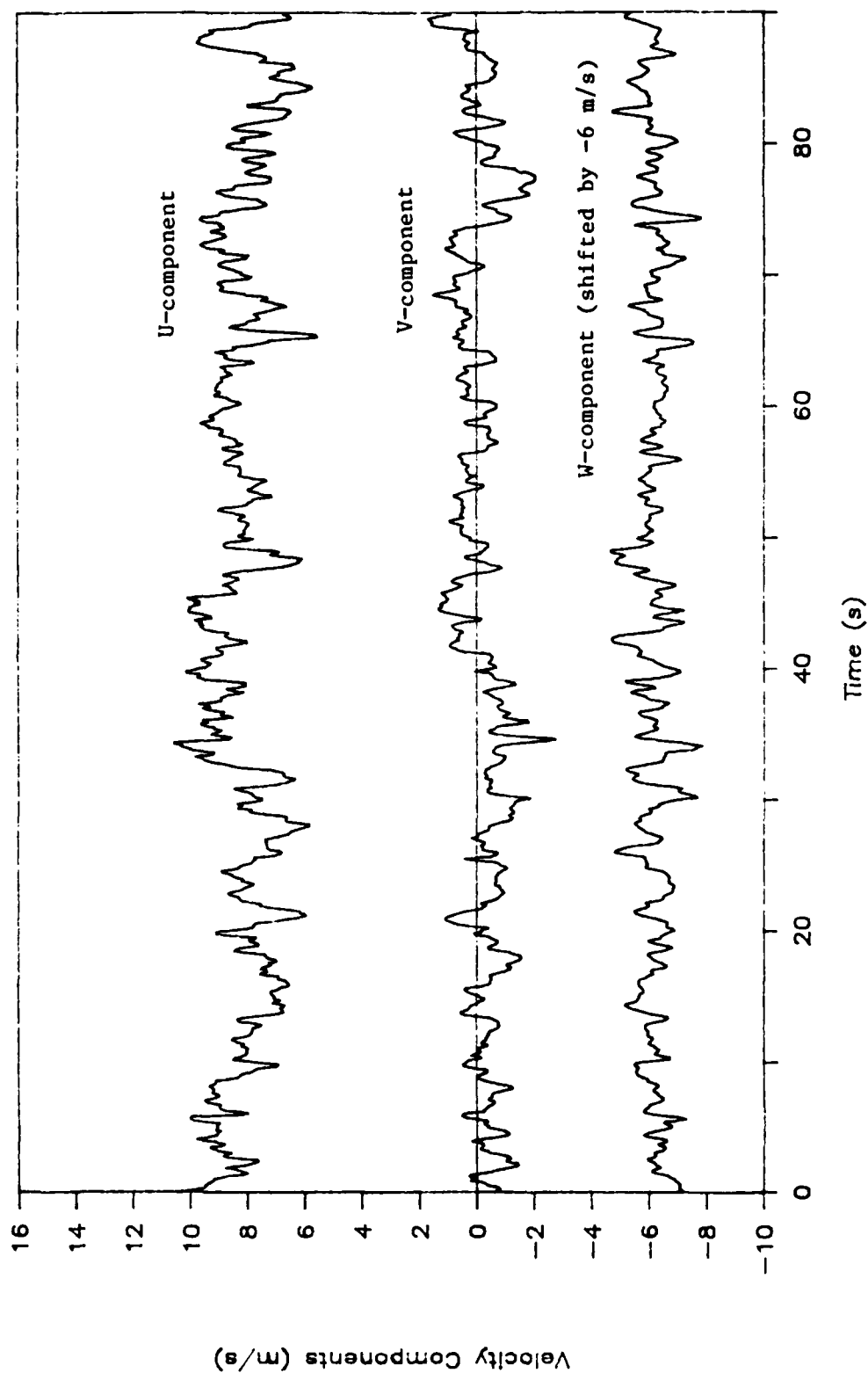


Figure 2. Time Series of Wind Components (0.1-s averages) Measured at the Ellensburg Airport.  
 $\bar{\alpha} = 3.4^\circ$ ,  $R_c = 318,000$ .

WRN4101/10 Hz

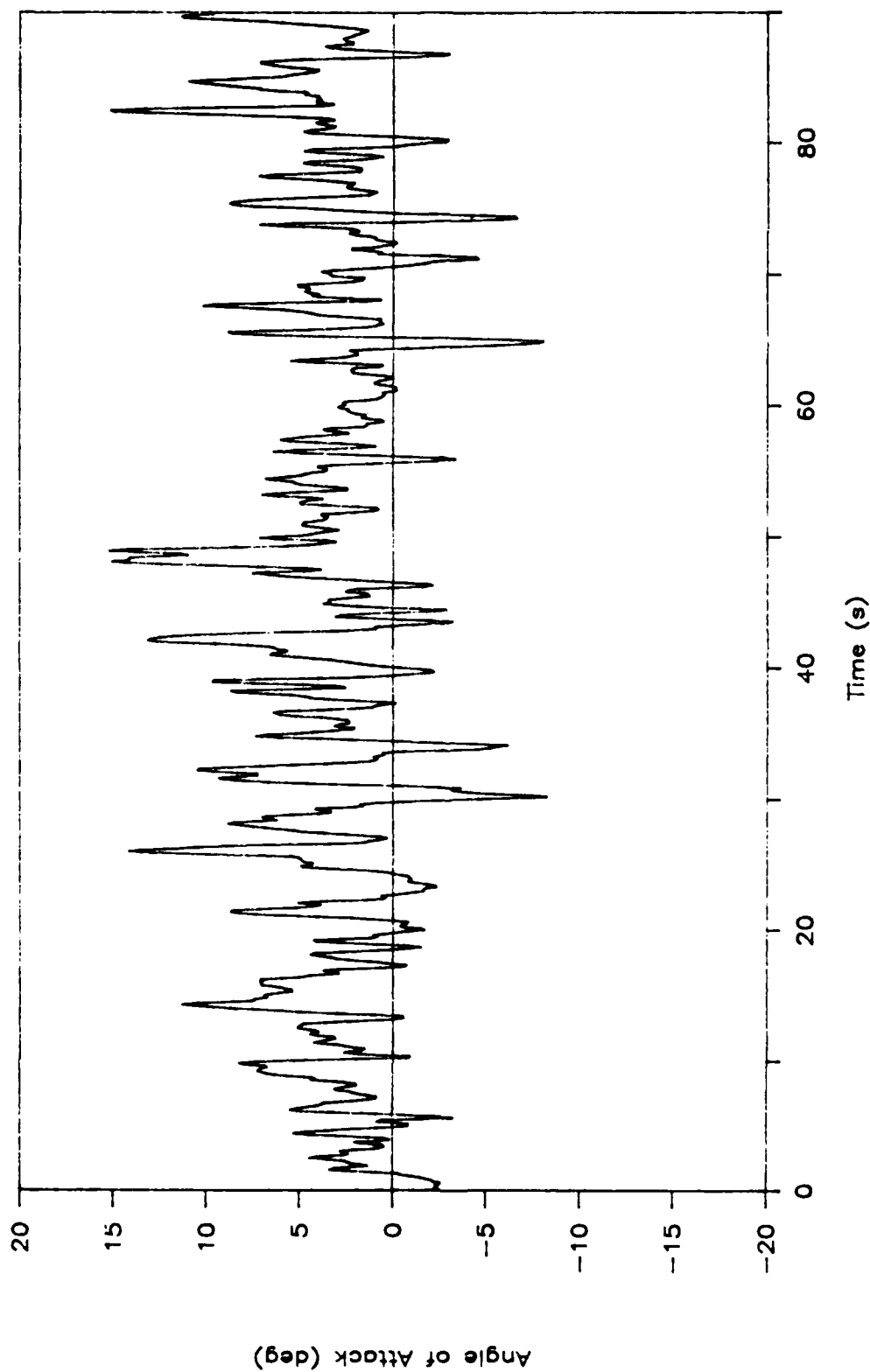


Figure 3. Time Series of Angles of Attack (0.1-s averages).  $\bar{\alpha} = 3.4^\circ$ ,  $R_C = 318,000$ .

WRN4101/10 Hz

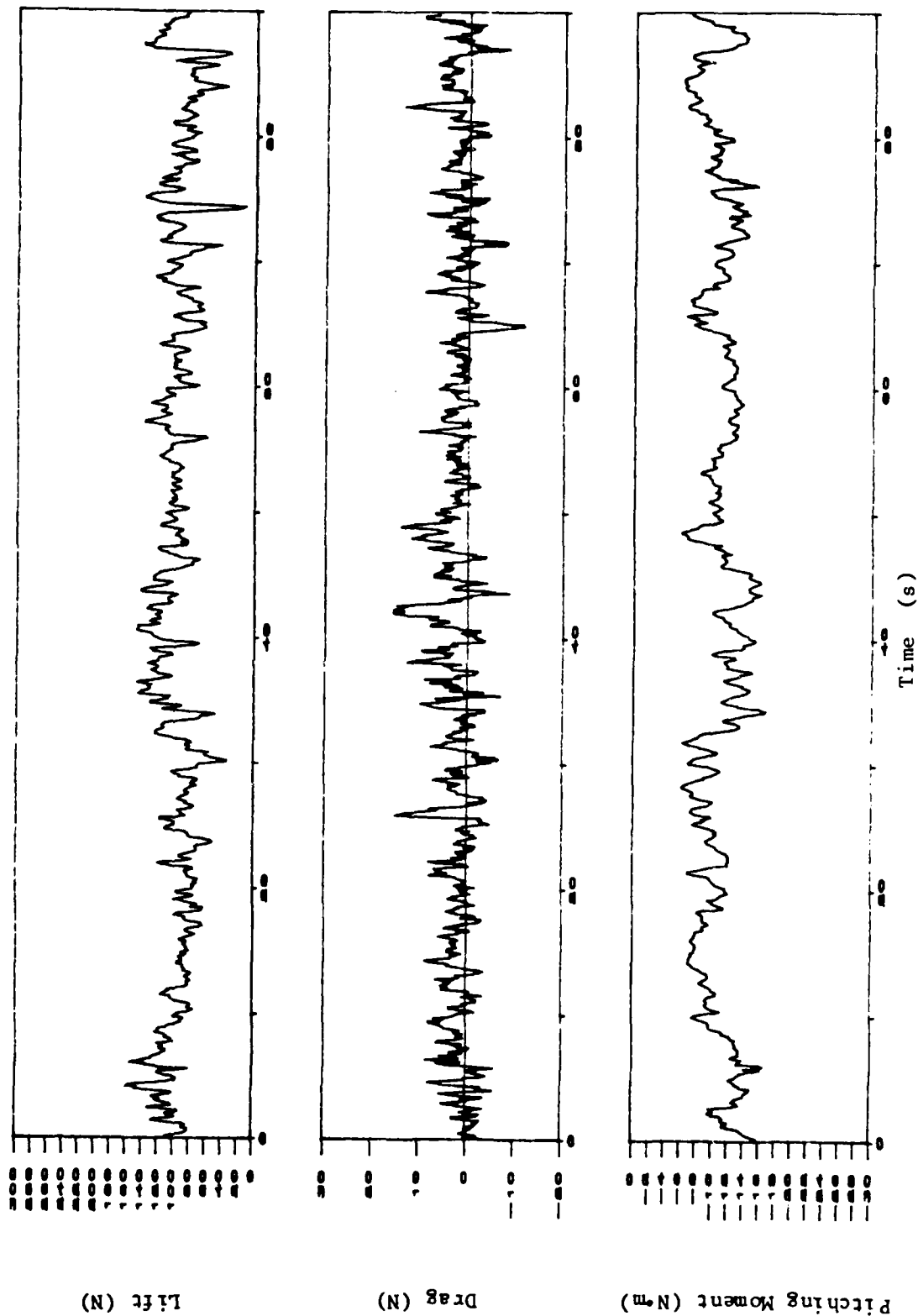


Figure 4. Time Series of Lift, Drag and Pitching Moment (0.1-s averages).  
 $\alpha = 3.4^\circ$ ,  $R_C = 318,000$ .

Table 1. Time-Averaged Ambient and Aerodynamic Parameters for the High  $R_c$  Series

RUN NO.	CL	CL'	CD	CD'	CN	CN'	U	U'	V	V'	W	W'	ALFA (deg)	Rc
33.01	1.82E+00	2.81E-01	2.19E-01	1.38E-01	-2.11E-01	4.27E-02	7.847990	0.910437	0.310896	1.237152	0.2115007	0.537362	1.61E+01	3.08E+05
33.02	1.73E+00	2.19E-01	1.38E-01	6.70E-02	-1.96E-01	2.47E-02	11.25016	1.193901	1.2822936	0.604113	-0.248107	0.594055	1.31E+01	4.46E+05
33.03	1.76E+00	2.35E-01	1.78E-01	9.46E-02	-2.01E-01	3.06E-02	9.153753	1.343375	1.0235184	1.451396	0.0269351	0.555833	1.48E+01	3.59E+05
33.04	1.74E+00	1.90E-01	1.59E-01	8.16E-02	-1.97E-01	1.94E-02	10.49213	0.844905	0.0935736	1.117092	-0.067970	0.689457	1.39E+01	4.16E+05
33.05	1.68E+00	2.00E-01	1.36E-01	6.19E-02	-1.90E-01	1.73E-02	10.57829	1.326489	-0.267797	1.139952	-0.259781	0.571195	1.31E+01	4.15E+05
33.06	1.64E+00	1.54E-01	1.53E-01	9.14E-02	-1.85E-01	1.69E-02	9.897160	1.145133	-0.442874	0.689762	-0.092354	0.632764	1.40E+01	3.93E+05
33.07	1.68E+00	2.02E-01	1.45E-01	9.98E-02	-1.92E-01	2.72E-02	9.139123	1.262176	0.6473952	0.608380	-0.209428	0.485851	1.32E+01	3.56E+05
33.08	1.62E+00	1.88E-01	1.39E-01	5.16E-02	-1.85E-01	1.44E-02	7.779105	0.667512	-0.635508	0.524865	-0.115519	0.406908	1.35E+01	3.06E+05
33.09	1.75E+00	2.24E-01	1.60E-01	9.20E-02	-1.99E-01	2.31E-02	10.32662	1.287170	0.2295144	1.042111	-0.098145	0.681837	1.39E+01	4.07E+05
34.01	1.56E+00	2.16E-01	1.10E-01	7.20E-02	-2.00E-01	1.85E-02	10.42659	1.367028	0.913638	0.895898	0.1603248	0.650321	1.05E+01	4.07E+05
34.02	1.55E+00	1.80E-01	1.16E-01	5.81E-02	-1.91E-01	1.73E+00	7.77581	0.772668	-0.363321	0.526084	0.2170176	0.448970	1.10E+01	3.06E+05
34.03	1.50E+00	2.48E-01	1.02E-01	8.22E-02	-1.99E-01	2.02E-02	10.60551	1.475536	0.2493264	0.804367	0.0218846	0.721766	9.69E+00	4.17E+05
34.04	1.41E+00	2.41E-01	7.83E-02	4.61E-02	-1.94E-01	1.58E-02	11.37848	1.091488	-0.501700	0.806500	-0.163982	0.630631	8.49E+00	4.47E+05
34.05	1.54E+00	2.37E-01	9.49E-02	6.23E-02	-1.96E-01	2.10E-02	11.08557	1.603248	0.3328416	1.037539	0.100584	0.662635	9.96E+00	4.35E+05
34.06	1.57E+00	2.23E-01	1.34E-01	8.51E-02	-2.03E-01	1.94E-02	10.68872	1.151534	-0.3533263	0.718108	0.3278428	0.815644	1.13E+01	4.19E+05
34.07	1.57E+00	2.92E-01	1.04E-01	8.15E-02	-2.03E-01	2.28E-02	10.30528	1.452981	1.3133832	0.977798	0.1002792	0.765352	1.01E+01	4.04E+05
34.08	1.53E+00	2.51E-01	8.57E-02	5.72E-02	-2.01E-01	1.91E-02	10.86368	1.055522	-0.211287	0.743712	-0.072268	0.618134	9.02E+00	4.25E+05
35.01	1.86E+00	1.52E-01	2.96E-01	1.38E-01	-2.27E-01	3.99E-02	10.54608	1.131722	0.9073896	0.860145	-0.033467	0.458845	1.92E+01	4.14E+05
35.02	1.84E+00	1.84E-01	2.52E-01	1.16E-01	-2.11E-01	3.78E-02	11.4681	0.941527	0.4901184	0.911047	-0.216712	0.642823	1.82E+01	4.49E+05
35.03	1.84E+00	1.98E-01	3.32E-01	1.80E-01	-2.36E-01	5.30E-02	10.12423	1.493536	0.8668512	0.841857	-0.05715	0.599541	1.90E+01	3.96E+05
35.04	1.89E+00	2.72E-01	3.05E-01	1.63E-01	-2.32E-01	4.90E-02	10.99552	2.027529	0.363204	1.114044	-0.122834	0.797966	1.89E+01	4.31E+05
35.05	1.86E+00	2.25E-01	3.18E-01	1.61E-01	-2.30E-01	4.99E-02	10.74938	1.682191	0.2690469	0.900988	0.0328269	0.684672	1.99E+01	4.21E+05
35.06	1.86E+00	1.82E-01	2.42E-01	9.90E-02	-2.14E-01	3.40E-02	11.60617	1.299667	0.0539496	0.798271	-0.296539	0.543458	1.79E+01	4.54E+05
35.07	1.89E+00	2.34E-01	3.20E-01	1.61E-01	-2.36E-01	5.09E-02	10.50218	1.573987	0.7860792	0.977188	0.0236829	0.599236	1.96E+01	4.12E+05
35.08	1.87E+00	1.68E-01	2.93E-01	1.66E-01	-2.27E-01	4.56E-02	11.52662	1.543812	0.6754368	0.893978	-0.123444	0.773582	1.89E+01	4.51E+05
36.01	7.33E-01	2.79E-01	1.61E-02	3.08E-02	-1.91E-01	1.79E-02	9.678314	1.399336	-0.150327	1.020470	-0.093268	1.020470	-1.08E+00	3.84E+05
36.02	6.89E-01	2.05E-01	5.81E-03	2.08E-02	-1.97E-01	1.60E-02	10.96914	1.004316	-0.271881	0.605942	-0.294436	0.553821	-2.24E+00	4.35E+05
36.03	7.52E-01	2.22E-01	4.82E-03	1.97E-02	-1.97E-01	1.67E-02	10.74176	1.400556	-0.343204	1.187196	-0.171328	0.497098	-1.40E+00	4.21E+05
36.04	9.68E-01	3.27E-01	2.92E-02	3.73E-02	-2.00E-01	1.96E-02	8.239353	0.895807	0.1594104	0.692810	0.3493008	0.508101	1.86E+00	3.27E+05
36.05	8.80E-01	3.05E-01	2.28E-02	3.54E-02	-2.01E-01	2.21E-02	9.161068	1.863547	-0.216895	1.123797	0.1506321	0.624535	5.15E-01	3.64E+05
36.06	8.54E-01	2.57E-01	2.05E-02	3.27E-02	-2.00E-01	1.65E-02	8.124139	1.020165	0.8147304	0.664768	0.1271016	0.430682	2.87E-01	3.22E+05
37.01	-1.91E-02	2.14E-01	1.37E-01	5.92E-02	-1.22E-01	5.15E-02	8.067141	1.368552	-0.502310	0.83058	0.0215493	0.475183	-1.05E+01	3.24E+05
37.02	-6.59E-02	2.06E-01	1.52E-01	7.67E-02	-1.08E-01	5.24E-02	8.739225	0.815644	-0.459028	0.826008	-0.114604	0.492252	-1.14E+01	3.47E+05
37.03	-9.04E-02	1.97E-01	1.67E-01	7.11E-02	-9.65E-02	5.71E-02	10.34948	1.302105	-0.269321	1.048664	-0.331713	0.630692	-1.25E+01	4.13E+05
37.04	-2.24E-02	2.08E-01	1.42E-01	6.70E-02	-1.21E-01	4.92E-02	9.443313	1.045464	0.2791968	0.799185	-0.089611	0.639470	-1.12E+01	3.77E+05
38.01	1.72E+00	3.13E-01	4.74E-01	2.08E-01	-2.70E-01	6.57E-02	8.973312	1.197254	-0.084124	0.8763	-0.214579	0.580034	2.30E+01	3.60E+05
38.02	1.72E+00	2.88E-01	6.99E-01	2.05E-01	-3.33E-01	6.20E-02	6.704076	0.695858	0.5937504	0.562356	0.3096768	0.436473	2.71E+01	2.70E+05
38.03	1.77E+00	3.22E-01	5.83E-01	2.28E-01	-3.02E-01	7.01E-02	7.4676	0.999744	0.6239256	1.061008	0.6239256	0.030876	2.47E+01	3.01E+05
38.04	1.80E+00	2.37E-01	5.90E-01	1.58E-01	-3.12E-01	4.30E-02	8.494776	0.827532	1.1664696	0.738530	0.827032	0.405993	2.47E+01	3.42E+05
38.05	1.73E+00	3.00E-01	5.49E-01	2.15E-01	-2.91E-01	6.28E-02	7.573670	1.107948	1.146048	0.683971	-0.011003	0.517245	2.44E+01	3.06E+05
38.06	1.68E+00	2.99E-01	5.90E-01	2.49E-01	-3.01E-01	7.20E-02	6.7056	0.82296	0.5596128	0.718718	0.0115824	0.518464	2.46E+01	2.72E+05
38.07	1.62E+00	3.09E-01	5.52E-01	2.12E-01	-2.88E-01	6.21E-02	7.501432	1.070000	0.5995720	0.780745	-0.019994	0.473354	2.43E+01	3.05E+05

Table 1. Time-Averaged Ambient and Aerodynamic Parameters for the High- $R_c$  Series (Cont.)

RUN NO.	CL	CL'	CD	CD'	CM	CM'	U	U'	V	V'	W	W'	ALFA (deg)	RC
39.01	1.48E+00	2.37E-01	7.59E-01	1.86E-01	-3.24E-01	5.24E-02	8.319304	0.953292	-0.164988	0.826099	-0.046116	0	2.93E+01	3.31E+05
39.02	1.59E+00	2.26E-01	7.69E-01	2.24E-01	-3.27E-01	5.40E-02	8.231428	0.849172	-0.849782	0.783031	-0.010668	0.655015	2.93E+01	3.30E+05
39.03	1.64E+00	3.09E-01	7.77E-01	2.51E-01	-3.39E-01	7.11E-02	8.703259	1.278331	-0.155600	1.229868	-0.162885	0.60198	2.85E+01	3.49E+05
39.04	1.34E+00	1.55E-01	6.47E-01	8.80E-02	-3.02E-01	2.80E-02	10.10412	0.886968	0.1246632	0.682142	-0.435559	0.3429	2.68E+01	4.03E+05
39.05	1.43E+00	2.24E-01	7.07E-01	2.18E-01	-3.11E-01	5.24E-02	9.00684	1.320393	-0.343601	0.688848	-0.227685	0.626668	2.82E+01	3.60E+05
39.06	1.50E+00	2.19E-01	8.13E-01	1.64E-01	-3.39E-01	4.90E-02	7.950098	0.830884	0.166116	0.574852	0.0941832	0.385267	3.00E+01	3.17E+05
39.07	1.51E+00	2.73E-01	8.00E-01	2.33E-01	-3.36E-01	6.13E-02	7.966557	1.175918	0.7629144	0.720547	0.0237439	0.579729	2.98E+01	3.16E+05
39.08	1.49E+00	2.43E-01	7.55E-01	1.67E-01	-3.29E-01	5.00E-02	8.484717	0.682752	0.0185928	0.848563	-0.067056	0.501700	2.88E+01	3.37E+05
40.01	-2.78E-01	1.11E-01	2.02E-01	6.10E-02	-3.30E-02	5.60E-02	9.457944	1.532839	0.620268	0.389839	-0.405079	0.554126	-1.78E+01	3.74E+05
40.02	-2.77E-01	1.27E-01	2.02E-01	6.63E-02	-3.34E-02	5.82E-02	9.541459	1.544208	0.620268	0.409468	-0.405018	0.564337	-1.78E+01	3.74E+05
40.03	-3.11E-01	1.04E-01	2.09E-01	5.90E-02	-2.81E-02	4.20E-02	9.087307	1.033881	-0.462686	0.74676	-0.325038	1.414272	-1.74E+01	3.57E+05
40.04	-3.00E-01	1.19E-01	2.00E-01	6.40E-02	-3.70E-02	4.50E-02	9.614916	0.762914	0.184404	0.671474	-0.259994	0.567842	-1.73E+01	3.78E+05
40.05	-3.04E-01	1.30E-01	2.05E-01	7.15E-02	-3.89E-02	4.89E-02	8.985504	1.072896	0.704088	0.667816	-0.250637	0.607161	-1.71E+01	3.53E+05
40.06	-2.69E-01	1.60E-01	1.85E-01	7.40E-02	-4.30E-02	4.90E-02	8.391753	0.855878	0.5050536	0.661111	-0.105156	0.505358	-1.63E+01	3.30E+05
40.07	-3.03E-01	1.54E-01	2.09E-01	7.65E-02	-3.27E-02	5.63E-02	8.699601	1.100632	-0.024323	0.743712	-0.293552	0.649925	-1.74E+01	3.42E+05
40.08	-3.60E-02	3.49E-01	1.14E-01	8.20E-02	-1.13E-01	6.50E-02	6.285585	0.787908	-0.309067	0.628497	0.4386072	0.551688	-1.14E+01	2.47E+05
41.01	1.14E+00	2.51E-01	2.47E-02	4.10E-02	-2.01E-01	1.89E-02	8.203692	0.938479	-0.166298	0.698296	-0.147370	0.479755	3.37E+00	3.18E+05
41.02	1.48E+00	4.02E-01	8.20E-02	7.10E-02	-2.08E-01	2.80E-02	7.630363	0.900074	-0.011582	0.704697	0.4547616	0.728776	8.09E+00	2.97E+05
41.03	1.20E+00	3.55E-01	2.98E-02	5.55E-02	-2.04E-01	2.54E-02	7.946745	1.175004	0.4821936	0.834847	-0.095524	0.564245	3.90E+00	3.08E+05
41.04	1.15E+00	2.80E-01	3.10E-02	3.80E-02	-2.02E-01	1.90E-02	8.760561	0.977188	-0.133197	0.638251	-0.112776	0.459028	3.69E+00	3.39E+05
41.05	1.26E+00	3.38E-01	3.52E-02	5.33E-02	-2.03E-01	2.35E-01	8.404688	1.281531	0.2309774	0.756056	0.0279196	0.590610	4.78E+00	3.26E+05
41.06	1.24E+00	2.90E-01	3.80E-02	5.80E-02	-2.04E-01	2.00E-02	7.708696	1.010107	0.7702296	0.612648	0.0435864	0.550773	4.80E+00	2.98E+05
41.07	1.16E+00	2.43E-01	3.11E-02	4.78E-02	-2.01E-01	1.45E-02	8.044703	1.339291	0.707898	0.646450	-0.120517	0.452231	3.75E+00	3.12E+05
41.08	1.07E+00	2.64E-01	1.80E-02	2.80E-02	-2.01E-01	1.50E-02	8.482584	0.921105	-0.448970	0.639470	-0.314248	0.389839	2.21E+00	3.28E+05
41.09	1.18E+00	3.15E-01	2.68E-02	4.90E-02	-2.05E-01	2.22E-02	8.633764	1.235049	-0.666597	1.495348	-0.138074	0.524957	3.53E+00	3.34E+05
42.01	2.68E-01	2.78E-01	2.65E-02	3.55E-02	-1.72E-01	3.29E-02	9.582607	1.492605	0.1990344	0.769924	-0.293217	0.575767	-7.27E+00	3.73E+05
42.02	2.73E-01	2.02E-01	2.50E-02	2.70E-02	-1.76E-01	2.70E-02	10.67379	1.182014	0.0103632	0.81534	-0.318516	0.672388	-7.25E+00	4.15E+05
42.03	3.33E-01	3.15E-01	2.22E-02	4.26E-02	-1.71E-01	3.50E-02	8.548420	1.003401	-0.117835	0.722254	-0.185318	0.539800	-6.88E+00	3.33E+05
42.04	2.01E-01	2.32E-01	3.40E-02	3.40E-02	-1.69E-01	3.70E-02	10.74389	1.131722	-0.355092	0.946708	-0.439521	0.523036	-7.99E+00	4.18E+05
42.05														
42.06	2.18E-01	2.52E-01	3.34E-02	3.53E-02	-1.65E-01	3.39E-02	10.42294	1.073200	0.4581144	0.711708	-0.384352	0.595884	-7.69E+00	4.05E+05
42.07	3.50E-01	2.81E-01	1.80E-02	3.37E-02	-1.79E-01	3.18E-02	9.3345	1.250594	0.5050536	0.885444	-0.169804	0.555071	-6.62E+00	3.63E+05
42.08	2.67E-01	2.31E-01	1.99E-02	3.25E-02	-1.68E-01	2.99E-02	11.41476	0.904646	0.2535936	0.619353	-0.344119	0.557784	-7.69E+00	4.44E+05
42.09	2.94E-01	2.62E-01	2.24E-02	3.23E-02	-1.75E-01	3.03E-02	9.677704	1.058600	0.2303373	1.058570	-0.238048	0.563849	-6.95E+00	3.76E+05

\*Wind speed components are in meters per second and the primes represent the standard deviations

moment correlate reasonably well with both  $U$  and  $\alpha$ , whereas the drag correlates better with  $\alpha$ . It is evident from the figures that the lift and the pitching moment follow the variations of the  $U$  component for both high- and low-frequency fluctuations. The  $W$  component or  $\alpha$  and the drag, on the other hand, consist of only relatively high frequency fluctuations. From now on, we emphasize only the dependence of the aerodynamic parameters on  $\alpha$ , which governs the unsteady aerodynamics and thus the dynamic stall phenomenon.

Note that the fluctuations in the drag result in instantaneous negative drag (i.e., propulsion). The drag becomes negative only when the vertical wind component or the angle of attack become negative, although the time-averaged drag is positive.<sup>8</sup> The exact mechanism that generates the instantaneous propulsion is not known. Under certain circumstances, however, the unsteady wind field could create a situation similar to that of a fish which manages its tail and fins to propel itself through unsteady flows around its body.

Figures 5 through 7 show the results for  $\bar{\alpha} = 19.9^\circ$ ,  $u'/\bar{U} = 0.156$ , and  $R_c = 420,900$ . For such large  $\alpha$ , the wing is in and out of dynamic stall repeatedly while the aerodynamic parameters vary drastically, as demonstrated by the highly fluctuating time series that consist of many sharp spikes. From Liu,<sup>8</sup> the time-averaged DSA for the Wortmann wing is estimated to be roughly  $19^\circ$  whereas the SSA of the Wortmann wing is between  $14^\circ$  to  $15^\circ$ , as derived from wind tunnel results.<sup>17,20</sup> Consider the part of a typical cycle when the  $W$  component, and thus  $\alpha$ , has reached the minimum and begins to increase again. At this point, the angle of attack is below the time-averaged DSA or even the SSA. The lift and drag increase with increasing  $\alpha$ , whereas the pitching moment changes insignificantly with  $\alpha$ . The same trend continues when  $\alpha$  exceeds the SSA but is below the DSA.

Drastic changes in the lift, drag and pitching moment take place when  $\alpha$  continues to increase and exceeds the DSA. The lift experiences a sudden drop as  $\alpha$  exceeds the DSA. When the amplitude of the fluctuation in  $\alpha$  is large, the sudden drop in the lift results in generating higher harmonics in the time series. The lift remains low for the rest of the cycle. Recovery of the lift does not take place until the end of the cycle as  $\alpha$  has gone through the maximum and returned to the initial value below the DSA. The drag time series shows different behaviors from that of the lift. In comparison, the drag increases with increasing  $\alpha$ ; it continues to increase when  $\alpha$  exceeds the DSA. The large spikes in the time series of the drag and  $\alpha$  are in phase, but those of the lift



WRN3505/10 Hz

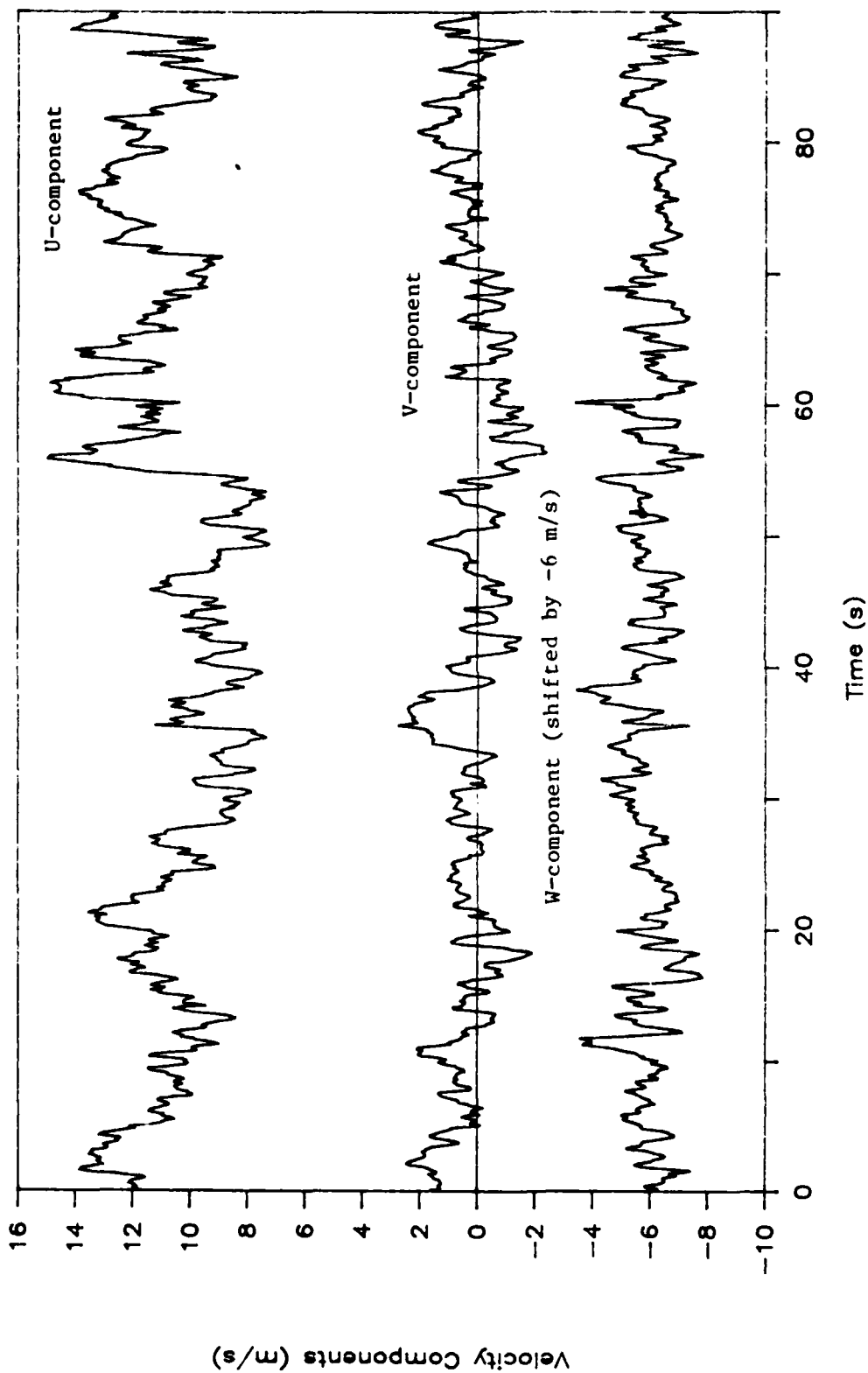


Figure 5. Time Series of Wind Components (0.1-s averages) Measured at the Ellensburg Airport.  
 $\alpha = 19.9^\circ$ ,  $R_c = 420,900$ .

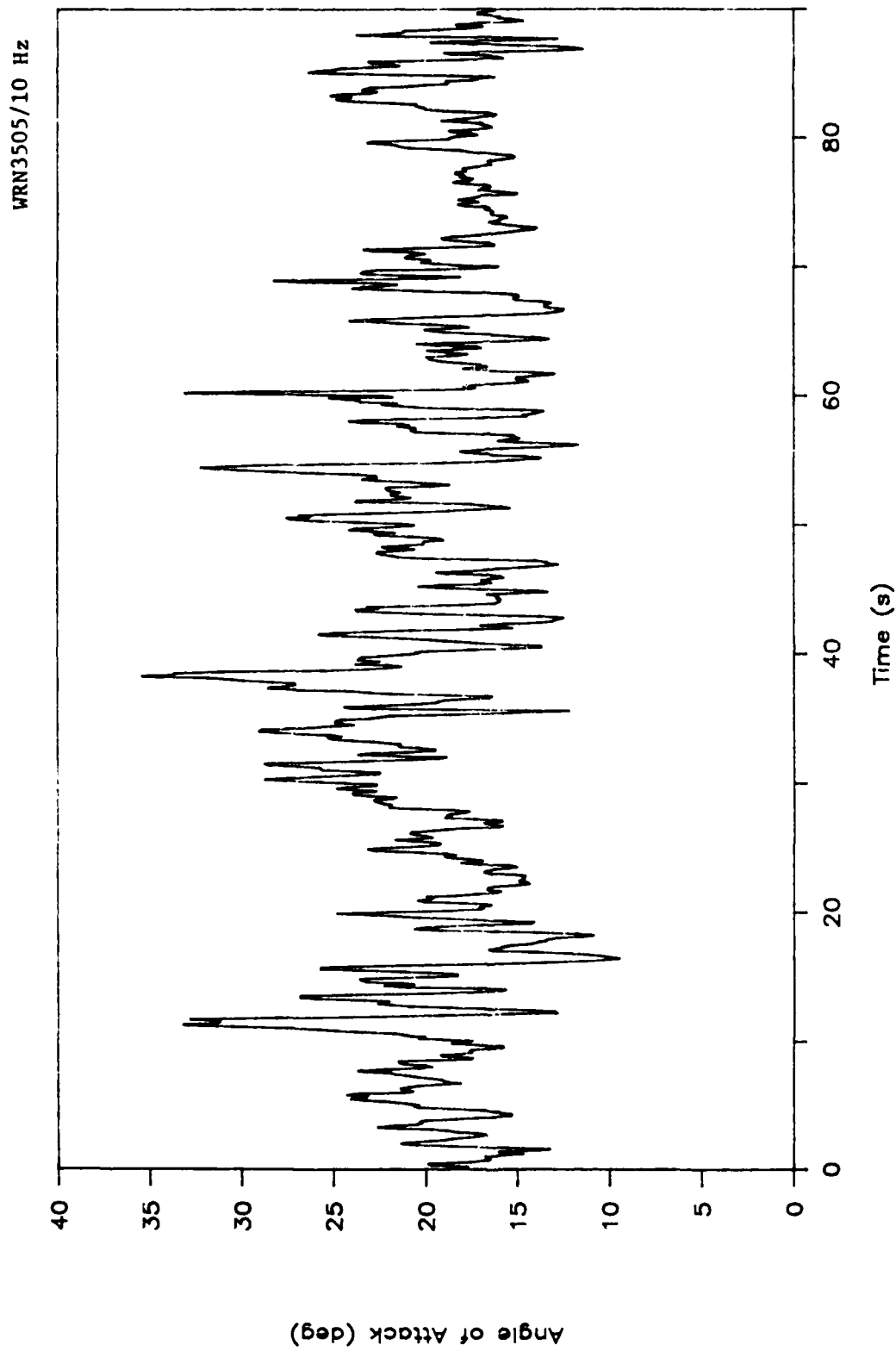


Figure 6. Time Series of Angles of Attack (0.1-s averages).  $\bar{\alpha} = 19.9^\circ$ ,  $R_c = 420,900$ .

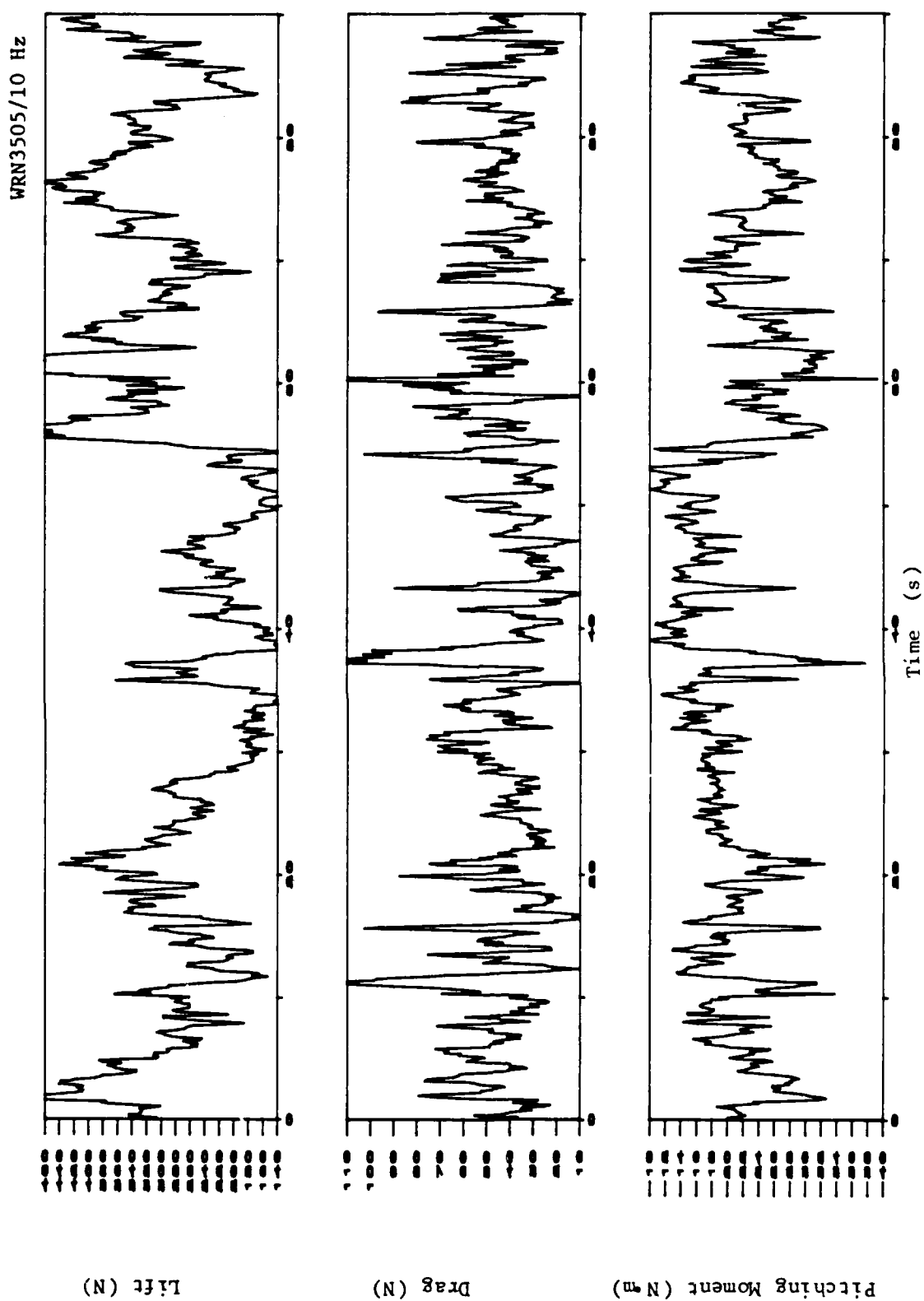


Figure 7. Time Series of Lift, Drag and Pitching Moment (0.1-s averages).  
 $\alpha = 19.9^\circ$ ,  $R_C = 420,900$ .

and drag are not in phase. The large spikes in lift are accompanied by the emergence of higher harmonics in the time series. The reduction of the drag to its original value takes place at the end of the cycle when  $\alpha$  returns to its initial value below the DSA. There also exists a hysteresis loop for the drag. The pitching moment does not change considerably for  $\alpha$  between  $3.4^\circ$  and the DSA, as can be seen from the near constant  $C_M$  in that range of  $\alpha$  (Figure 8 in Reference 8). As the DSA is exceeded, the pitching moment drops rapidly, in the form of negative spikes shown in the time series. Note that the contribution of the lift is larger than that of the drag, for the Wortmann wing, due to a relatively large moment arm of the former (to the quarter chord).

Figures 8 through 10 illustrate the results for  $\alpha = 23.0^\circ$ ,  $u'/U = 0.13$ , and  $R_c = 360,000$ . For this run,  $\alpha$  is about  $3^\circ$  higher than the time-averaged DSA. Comparison of the aerodynamic parameters shows that there are more large-amplitude jumps in the lift time series for  $\alpha = 23.0^\circ$  than for  $\alpha = 19.9^\circ$ . The corresponding average and root-mean-square (rms) lift coefficients are  $C_L = 1.72$  and  $C_L' = 0.31$  for  $\alpha = 23.0^\circ$  and  $C_L = 1.86$  and  $C_L' = 0.23$  for  $\alpha = 19.9^\circ$  (see Table 2). The drag and pitching moment time series of the two runs show similar characteristics. From Table 2, the average and rms coefficients are  $C_D = 0.47$ ,  $C_D' = 0.21$ ,  $C_M = -0.27$  and  $C_M' = 0.066$  for  $\alpha = 23.0^\circ$  and  $C_D = 0.31$ ,  $C_D' = 0.16$ ,  $C_M = -0.23$  and  $C_M' = 0.050$  for  $\alpha = 19.9^\circ$ . The above comparison indicates that the wing is, on the average, dynamically stalled (light stall, see Reference 10) more often for  $\alpha = 23.0^\circ$  than for  $\alpha = 19.9^\circ$ , as anticipated.

Figures 11 through 13 show the results for  $\alpha = 29.3^\circ$ ,  $u'/U = 0.12$ , and  $R_c = 331,000$ . The Wortmann wing is in deep stall (see Reference 20) most of the time. The time series of the aerodynamic parameters show a significant reduction in the number density of large-amplitude spikes. The coefficients are  $C_L = 1.48$ ,  $C_L' = 0.24$ ,  $C_D = 0.76$ ,  $C_D' = 0.19$ ,  $C_M = -0.32$  and  $C_M' = 0.052$ , respectively. Here, the lift coefficient reduces significantly, whereas the drag coefficient continues to increase, from their values before dynamic stall takes place. Some reductions in the rms coefficients are evident, but the values of these coefficients remain reasonably high.

In summary, the results presented here, together with those presented previously by Liu,<sup>8</sup> show that the unsteady wind field at 6 m above the ground reduces the minimum drag coefficient of the Wortmann wing (from about 0.05 to

WRN3801/10 Hz

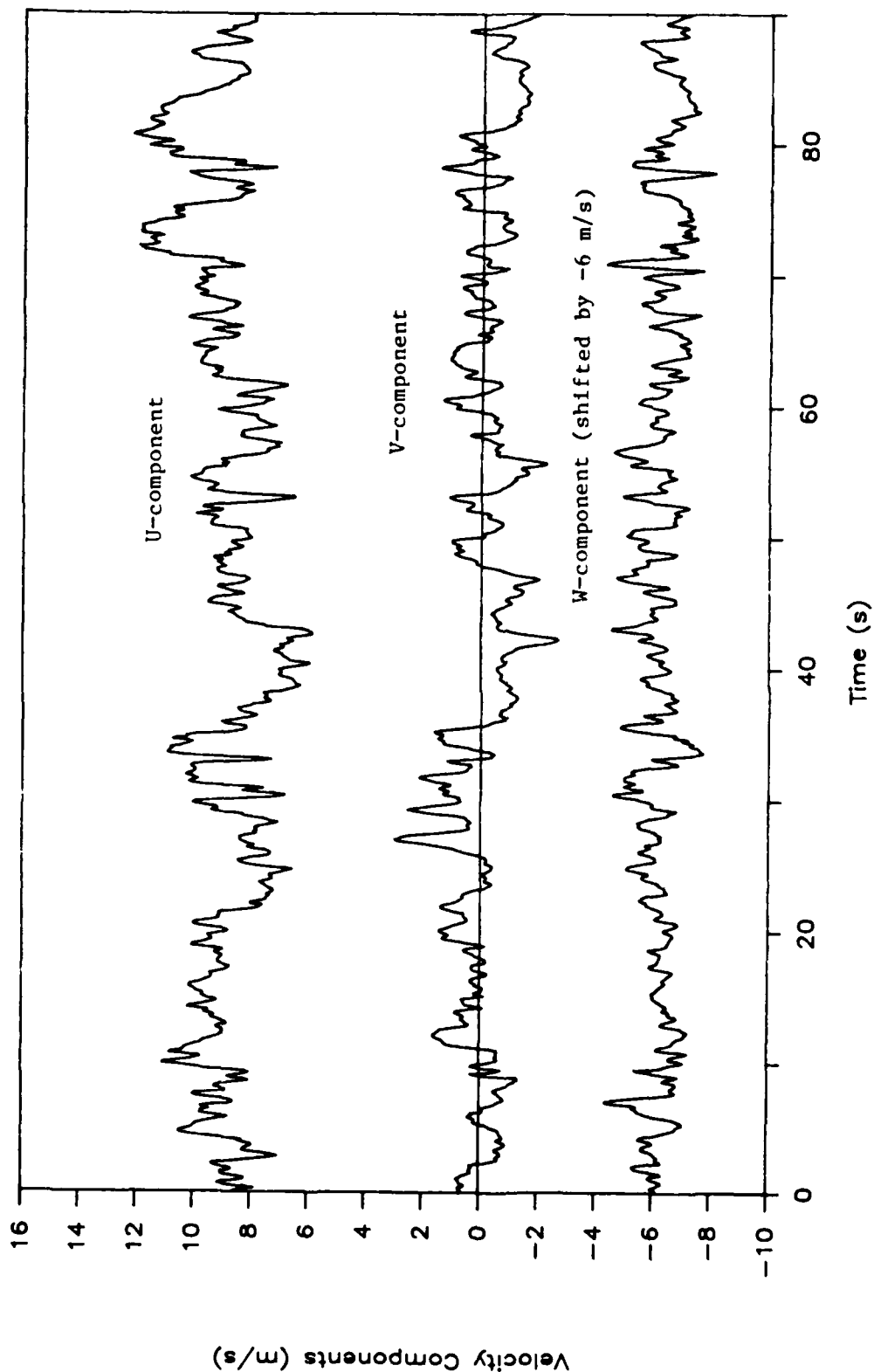


Figure 8. Time Series of Wind Components (0.1-s averages) Measured at the Ellensburg Airport.  
 $\alpha = 23.0^\circ$ ,  $R_c = 360,000$ .

WRN3801/10 Hz

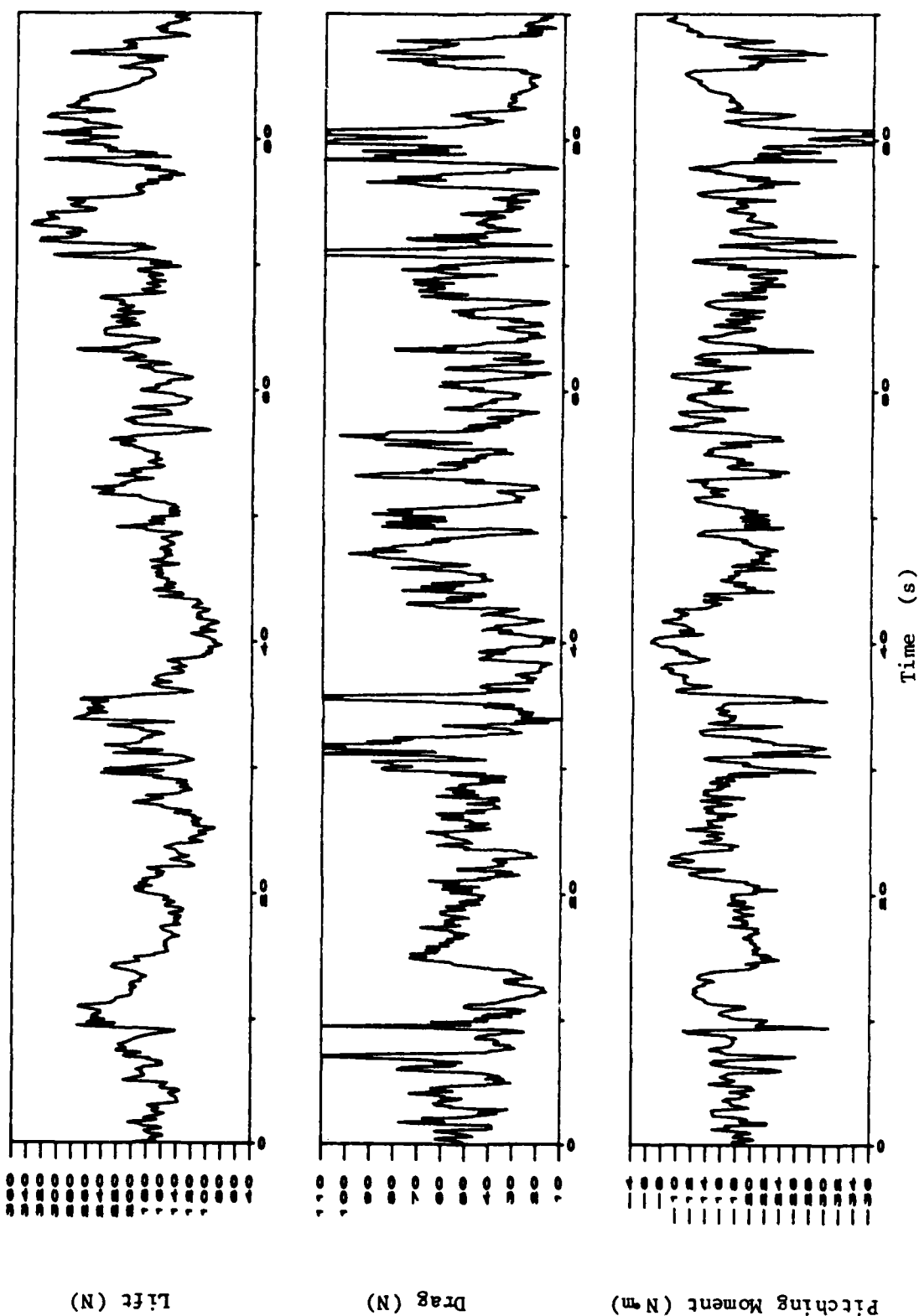


Figure 10. Time Series of Lift, Drag and Pitching Moment (0.1-s averages).  
 $\alpha = 23.0^\circ$ ,  $R_c = 360,000$ .

WRN3801/10 Hz

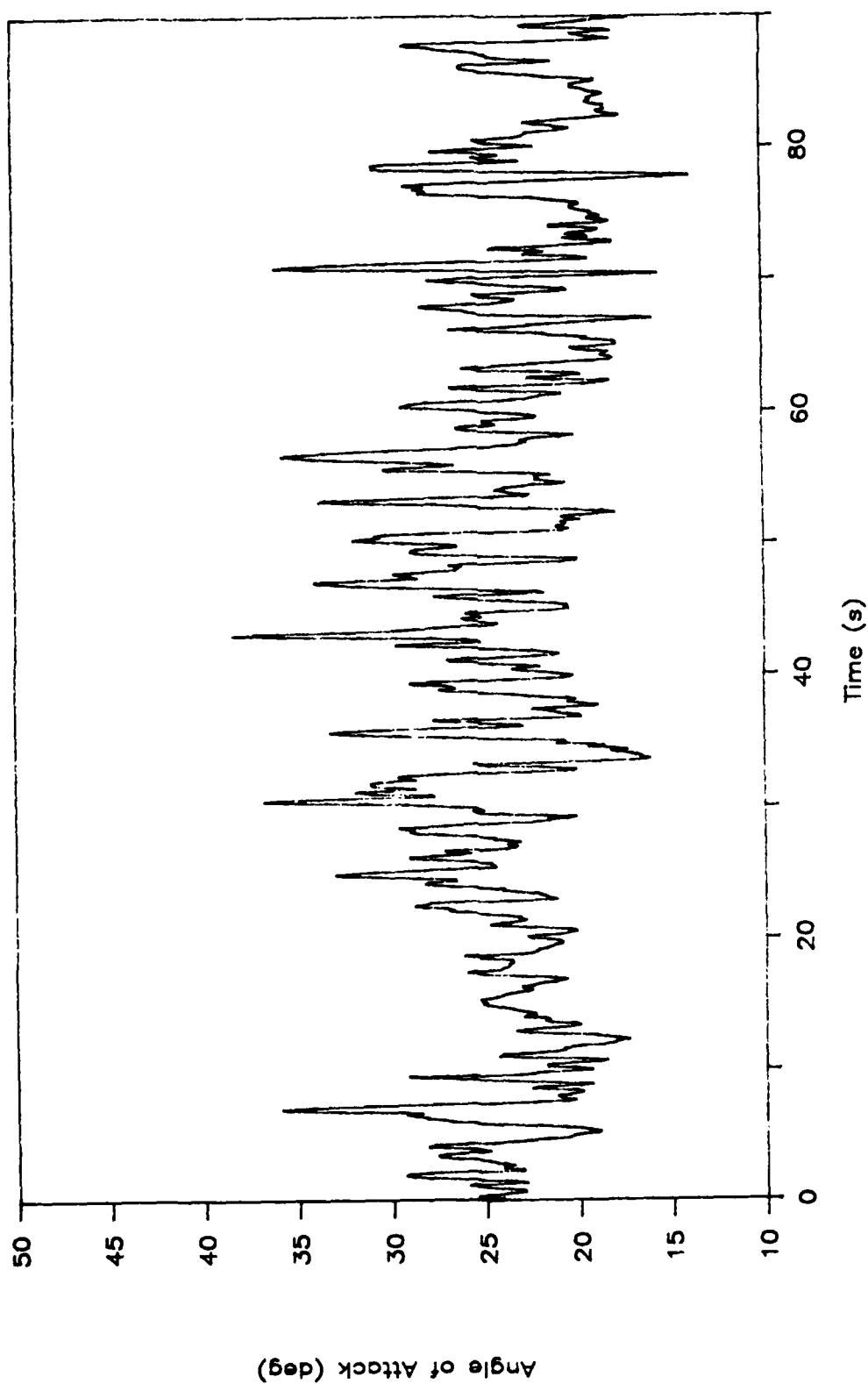


Figure 9. Time Series of Angles of Attack (0.1-s averages).  $\bar{\alpha} = 23.0^\circ$ ,  $R_c = 360,000$ .

Table 2. Time-Averaged Ambient and Aerodynamic Parameters for the Low- $R_c$  Series

RUN NO.	CL	CL'	CD	CD'	CM	CM'	U	U'	V	V'	W	W'	ALFA (deg)	Rc
20.01	1.03E+00	4.93E-01	9.05E-02	1.09E-01	-1.75E-01	4.44E-02	3.04E+00	6.50E-01	-9.34E-01	6.64E-01	8.32E-02	3.25E-01	5.76E+00	1.27E+05
20.02	1.06E+00	3.38E-01	1.03E-01	7.67E-02	-1.71E-01	5.03E-02	2.99E+00	6.92E-01	5.36E-01	2.75E-01	1.16E-01	2.40E-01	6.39E+00	1.25E+05
20.03	1.03E+00	7.38E-01	1.04E-01	1.26E-01	-2.21E-01	7.43E-02	3.21E+00	6.30E-01	4.93E-01	6.50E-01	-3.57E-02	3.62E-01	4.38E+00	1.33E+05
20.04	9.63E-01	6.45E-01	1.03E-01	1.55E-01	-1.91E-01	4.60E-02	3.94E+00	5.60E-01	-8.17E-01	4.75E-01	-1.44E-02	3.92E-01	4.52E+00	1.63E+05
21.01	-3.30E-01	7.16E-01	3.95E-01	3.11E-01	-1.09E-02	1.30E-01	2.05E+00	3.60E-01	4.34E-01	3.69E-01	-2.72E-01	4.29E-01	-1.37E+01	8.63E+04
21.03	-4.00E-02	5.52E-01	1.57E-01	1.38E-01	-6.88E-02	7.90E-02	2.16E+00	8.70E-01	7.16E-02	5.33E-01	-4.48E-02	3.84E-01	-5.53E+00	8.97E+04
22.06	1.55E+00	5.83E-01	2.00E-01	2.72E-01	-2.29E-01	7.82E-02	2.69E+00	6.28E-01	-3.38E-02	5.90E-01	-7.89E-02	4.25E-01	1.27E+01	1.11E+05
23.01	-1.21E-01	4.61E-01	1.36E-02	4.35E-02	-7.65E-02	2.99E-02	2.37E+00	3.70E-01	9.81E-03	2.45E-01	-2.97E-01	1.85E-01	-3.38E+00	9.56E+04
24.01	1.70E+00	2.70E-01	2.75E-01	2.65E-01	-2.19E-01	5.24E-02	4.21E+00	4.75E-01	-2.72E-02	5.75E-01	-1.55E-01	5.61E-01	1.73E+01	1.68E+05
24.02	1.64E+00	5.77E-01	3.76E-01	6.55E-01	-2.35E-01	1.40E-01	2.90E+00	5.54E-01	-6.36E-01	3.03E-01	-2.53E-01	5.57E-01	1.62E+01	1.17E+05
24.03	1.65E+00	1.77E-01	1.42E-01	5.10E-02	-1.80E-01	1.70E-02	4.59E+00	3.20E-01	-3.78E-02	4.48E-01	-4.27E-01	1.72E-01	1.38E+01	1.83E+05
24.04	1.83E+00	6.91E-01	5.38E-01	6.13E-01	-2.92E-01	1.28E-01	2.58E+00	9.46E-01	4.18E-01	9.27E-01	3.84E-02	5.73E-01	2.21E+01	1.05E+05
24.05	1.70E+00	7.10E-01	2.84E-01	2.52E-01	-2.19E-01	6.19E-02	3.36E+00	6.68E-01	-2.11E-01	6.80E-01	-2.83E-01	4.35E-01	1.52E+01	1.35E+05
24.06	1.34E+00	3.17E-01	8.09E-02	8.62E-02	-1.92E-01	2.48E-02	2.92E+00	3.00E-01	5.14E-01	2.86E-01	-5.16E-01	2.90E-01	9.21E+00	1.18E+05
24.07	1.98E+00	1.55E+00	8.52E-01	8.64E-01	-3.62E-01	2.83E-01	2.09E+00	6.26E-01	-2.07E-01	8.33E-01	-2.85E-01	5.53E-01	2.84E+01	8.61E+04
26.01	1.21E+00	2.59E-01	9.95E-02	7.80E-02	-1.74E-01	2.62E-02	4.07E+00	3.47E-01	-6.66E-01	4.97E-01	-2.76E-01	3.47E-01	1.03E+01	1.73E+05
26.02	1.24E+00	3.37E-01	1.08E-01	9.60E-02	-1.57E-01	2.85E-02	4.07E+00	4.36E-01	-4.51E-01	3.11E-01	-2.11E-01	3.32E-01	1.10E+01	1.73E+05
26.03	9.57E-01	2.68E-01	8.11E-02	5.25E-02	-1.66E-01	2.95E-02	3.34E+00	6.36E-01	-2.75E-01	2.16E-01	-3.58E-01	2.69E-01	8.21E+00	1.43E+05
26.04	1.50E+00	2.86E-01	1.42E-01	1.09E-01	-1.88E-01	3.70E-02	4.50E+00	6.28E-01	7.19E-02	5.58E-01	-1.52E-01	3.85E-01	1.25E+01	1.91E+05
26.05	1.31E+00	2.65E-01	7.14E-02	9.31E-02	-1.64E-01	2.23E-02	3.42E+00	2.04E-01	-4.85E-01	5.12E-01	-2.14E-01	2.99E-01	1.06E+01	1.45E+05
26.06	1.61E+00	3.16E-01	1.60E-01	1.38E-01	-1.82E-01	3.00E-02	4.52E+00	4.96E-01	-2.01E-01	3.28E-01	-1.91E-02	3.36E-01	1.41E+01	1.91E+05
26.07	1.42E+00	3.45E-01	7.89E-02	1.57E-01	-1.77E-01	3.49E-02	2.75E+00	3.53E-01	2.64E-01	4.68E-01	-1.32E-01	3.46E-01	1.15E+01	1.17E+05
26.08	2.12E+00	7.38E-01	2.58E-01	1.13E-01	-2.70E-01	8.09E-02	4.33E+00	7.89E-01	3.54E-03	5.87E-01	8.38E-02	6.84E-01	1.51E+01	1.81E+05
26.10	1.37E+00	4.21E-01	5.87E-02	7.94E-02	-1.97E-01	4.76E-02	4.28E+00	4.42E-01	-1.21E-01	6.79E-01	-3.90E-01	5.56E-01	8.80E+00	1.80E+05
26.11	1.56E+00	6.72E-01	1.85E-01	1.16E-01	-2.18E-01	1.01E-01	3.46E+00	5.63E-01	-2.87E-01	5.29E-01	4.79E-02	5.55E-01	1.48E+01	1.45E+05
26.12	1.53E+00	5.21E-01	1.46E-01	1.21E-01	-2.12E-01	3.36E-02	4.65E+00	4.74E-01	-4.40E-01	8.22E-01	-2.65E-01	4.62E-01	1.12E+01	1.97E+05
26.13	1.36E+00	1.60E-01	5.98E-02	5.87E-02	-1.85E-01	2.74E-02	4.78E+00	3.94E-01	-5.06E-02	2.82E-01	-4.72E-01	2.72E-01	8.49E+00	2.02E+05
26.14	1.23E+00	3.29E-01	7.16E-02	1.23E-01	-1.52E-01	4.99E-02	3.75E+00	7.89E-01	-4.05E-01	4.66E-01	-8.56E-02	3.77E-01	1.23E+01	1.59E+05
26.15	1.24E+00	2.95E-01	6.68E-02	6.05E-02	-1.57E-01	2.99E-02	3.86E+00	5.17E-01	-3.44E-01	4.85E-01	-2.33E-01	2.26E-01	1.04E+01	1.63E+05
26.16	1.13E+00	3.07E-01	5.55E-02	4.53E-02	-1.59E-01	3.20E-02	4.40E+00	4.16E-01	-4.62E-01	5.40E-01	-3.58E-01	2.58E-01	9.41E+00	1.84E+05
28.02	2.16E-01	2.72E-01	4.65E-02	4.04E-02	-1.51E-01	4.73E-02	4.01E+00	5.17E-01	7.89E-02	2.43E-01	-1.21E-01	3.20E-01	-2.35E+00	1.72E+05
28.03	-7.87E-02	2.66E-01	4.91E-02	2.90E-02	-8.43E-02	4.06E-02	2.74E+00	1.97E-01	-4.37E-01	3.38E-01	-1.94E-01	1.25E-01	-4.98E+00	1.18E+05
28.05	1.73E-01	3.12E-01	3.51E-02	4.18E-02	-1.19E-01	4.30E-02	4.13E+00	3.88E-01	-5.85E-03	4.27E-01	-1.80E-01	3.34E-01	-3.22E+00	1.78E+05
28.06	7.81E-01	3.08E-01	4.51E-02	7.01E-02	-1.23E-01	2.85E-02	2.87E+00	4.14E-01	-6.85E-01	3.29E-01	4.61E-01	3.99E-01	8.22E+00	1.25E+05
29.01	1.67E+00	5.01E-01	4.21E-01	3.16E-01	-2.20E-01	8.15E-02	3.34E+00	4.51E-01	2.93E-02	5.00E-01	-1.62E-01	3.47E-01	2.19E+01	1.43E+05
29.04	1.94E+00	4.66E-01	4.80E-01	3.10E-01	-2.53E-01	7.19E-02	3.62E+00	6.21E-01	-4.09E-01	6.64E-01	-1.21E-01	3.98E-01	2.21E+01	1.55E+05
29.05	1.41E+00	3.11E-01	4.32E-01	1.80E-01	-2.02E-01	5.95E-02	3.13E+00	3.12E-01	5.06E-01	5.50E-01	-6.31E-02	2.41E-01	2.30E+01	1.33E+05
29.06	1.94E+00	5.55E-01	8.43E-01	4.83E-01	-3.07E-01	9.85E-02	3.17E+00	5.67E-01	8.47E-03	4.85E-01	-2.64E-01	4.65E-01	2.99E+01	1.37E+05
29.07	1.53E+00	4.99E-01	2.39E-01	2.98E-01	-1.78E-01	7.85E-02	3.09E+00	5.40E-01	-1.02E+00	4.93E-01	-5.11E-01	4.35E-01	1.50E+01	1.34E+05
29.08	1.43E+00	2.99E-01	3.43E-01	2.49E-01	-1.77E-01	6.00E-02	3.32E+00	1.87E-01	-4.88E-01	3.64E-01	-2.22E-01	4.15E-01	2.04E+01	1.43E+05



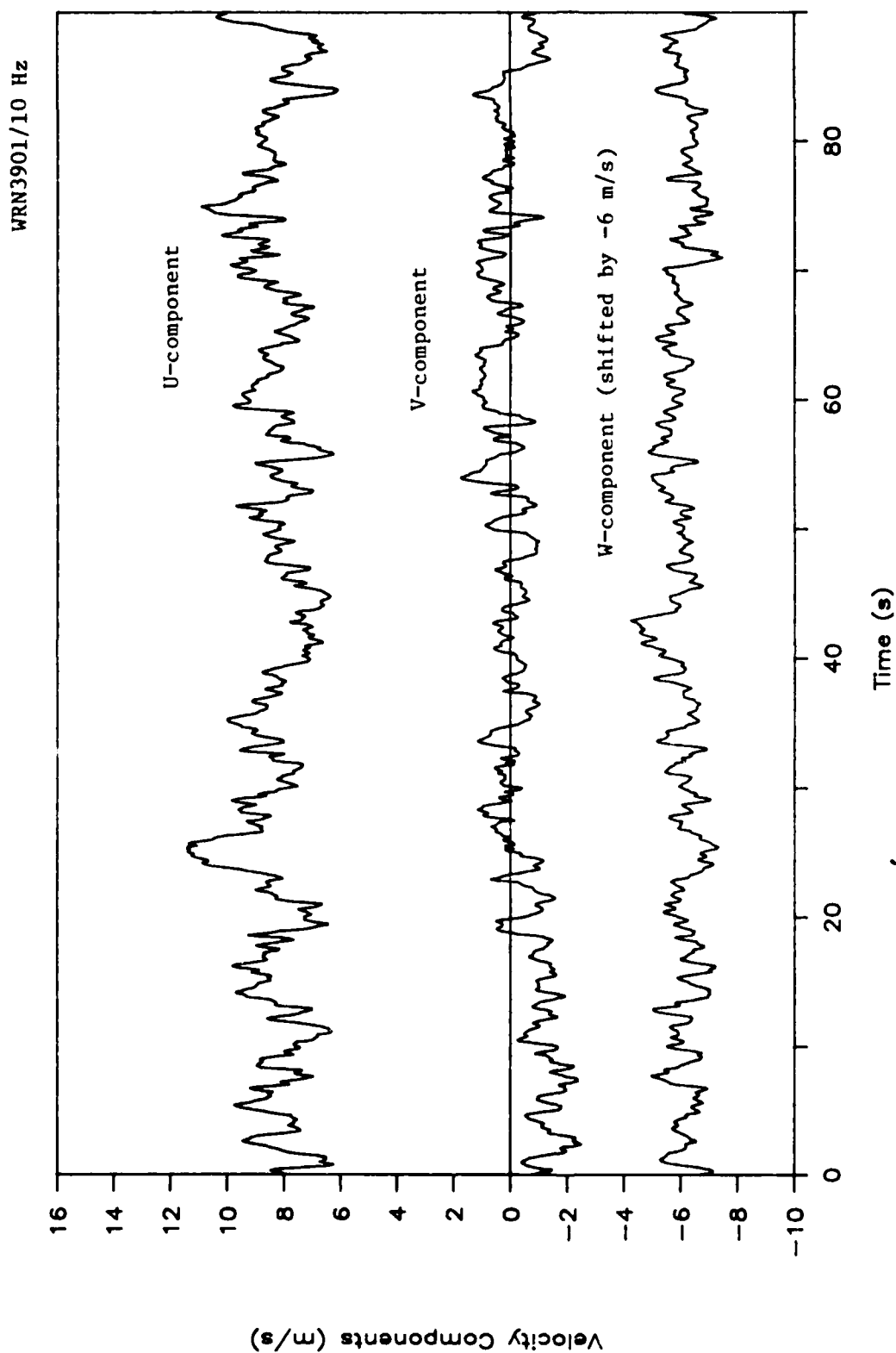


Figure 11. Time Series of Wind Components (0.1-s averages) Measured at the Ellensburg Airport.  
 $\alpha = 29.3^\circ$ ,  $R_c = 331,000$ .

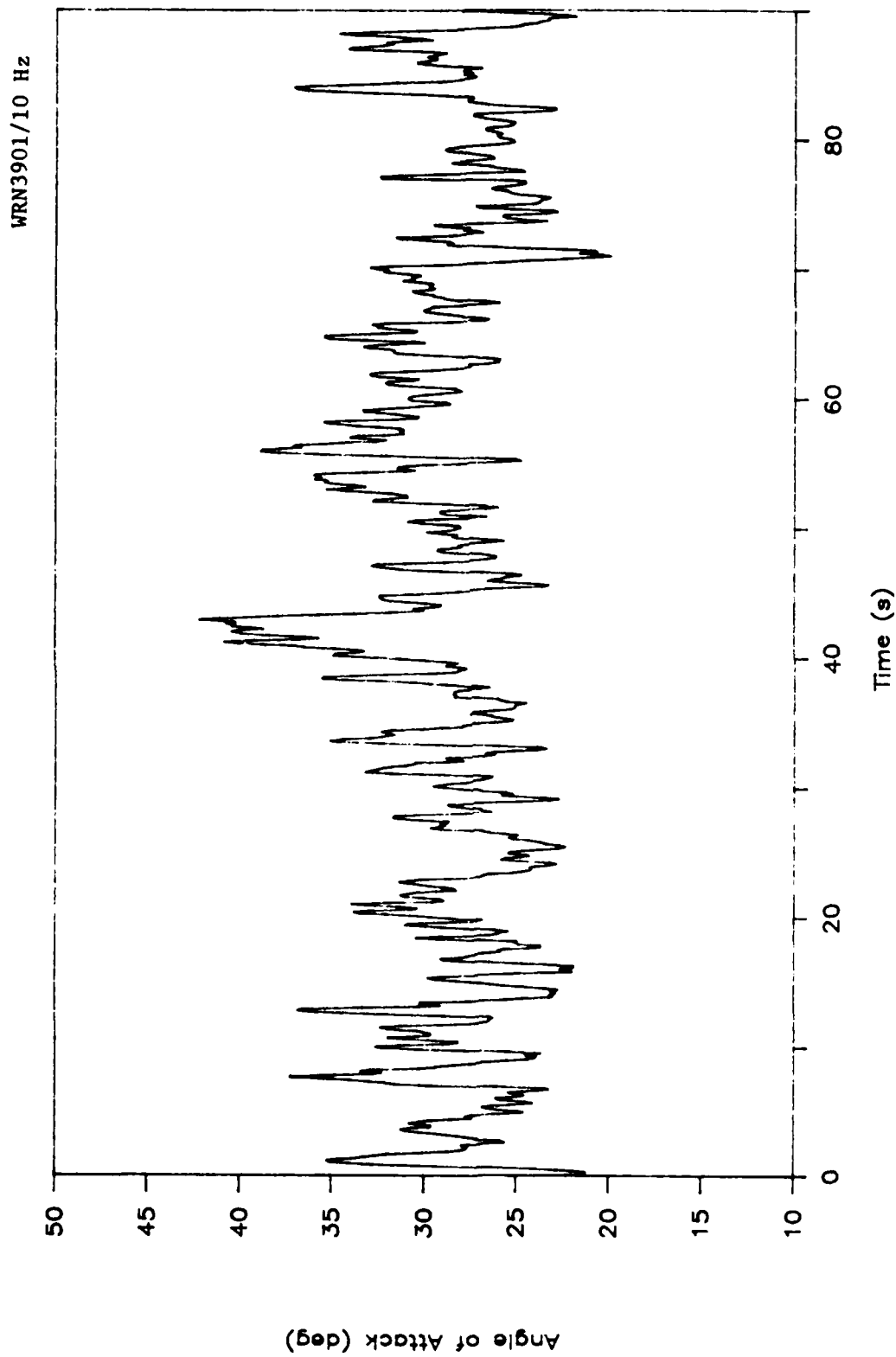


Figure 12. Time Series of Angles of Attack (0.1-s averages).  $\bar{\alpha} = 29.3^\circ$ ,  $R_C = 331,000$ .

WRN3901/10 Hz

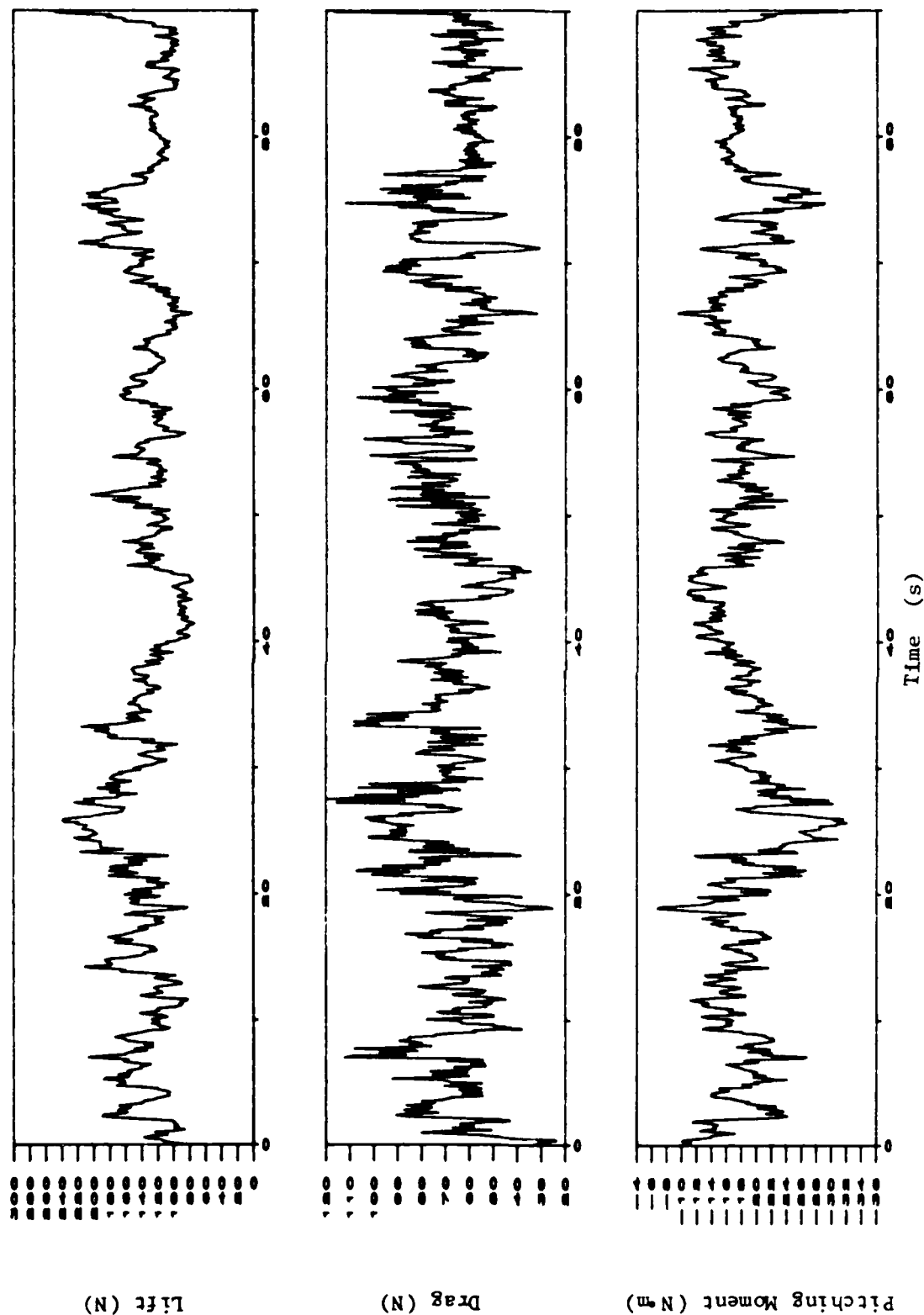


Figure 13. Time Series of Lift, Drag and Pitching Moment (0.1-s averages).  
 $\alpha = 29.3^\circ$ ,  $R_c = 331,000$ .

0.025) at small  $\alpha$  and increases the maximum lift coefficient (from about 1.6 to 1.9) at large  $\alpha$  beyond the SSA and below the DSA. Wind tunnel data (see, for example, Reference 4) using the same wing model in a steady air flow were used as a reference for the present full-scale results. The SSA and the DSA are measured to be about  $14^\circ$  to  $15^\circ$ <sup>17,21</sup> and  $19^\circ$ ,<sup>8</sup> respectively. For  $\alpha$  exceeding the dynamic stall angle, referred to as light stall,<sup>10</sup> the time series of the aerodynamic parameters are characterized by highly fluctuating signals with large-amplitude spikes. The average  $C_L$  decreases slightly, and  $C_D$  continues to increase from the values before dynamic stall.  $C_M$  remains nearly constant from  $\bar{\alpha} = 0^\circ$  to  $15^\circ$  and begins to decrease for  $\alpha$  exceeding the DSA. The rms coefficients of the fluctuating force are usually highest under light stall conditions. For deep stall with  $\alpha$  greatly exceeding the DSA,  $C_L$  and  $C_M$  continue to decrease, whereas  $C_D$  increases. The rms coefficients decrease somewhat but their values remain relatively high.

#### Hysteresis Loops of Aerodynamic Coefficients

The unsteady coefficients of lift, drag and pitching moment of nine selected cycles from the time series with relatively large amplitudes of the fluctuating  $\alpha$  are shown in Figures 14 through 22. In each group of figures, we illustrate the lift, drag and moment coefficients as the ordinate versus the instantaneous angle of attack as the abscissa for three individual cycles with  $\bar{\alpha} = 3.4^\circ$ ,  $19.9^\circ$  and  $29.3^\circ$ . The corresponding time-averaged coefficients are plotted as a dashed curve in each figure. The shapes of the loops appear to be considerably different for each individual cycle. However, there are some common, organized features in these cycles. Efforts are made to examine the hysteresis loops in these coefficients and to compare them with wind tunnel results for an oscillating airfoil. It is important to bear in mind that there are basic differences in the wind tunnel and EATS experiments. The unsteadiness of the present experiments is due entirely to the wind field consisting of eddies with a wide spectrum of sizes and frequencies. The wind tunnel experiments,<sup>12,13</sup> on the other hand, were conducted with a pitching or plunging airfoil oscillating at a single frequency in a steady air flow with a certain turbulence level inherent to the wind tunnels. Specifically, the unsteadiness of the present experiments is due to the variations in all three wind components. The net result is to introduce a combined unsteady motion that includes streamwise translating, spanwise sweeping, pitching and plunging components

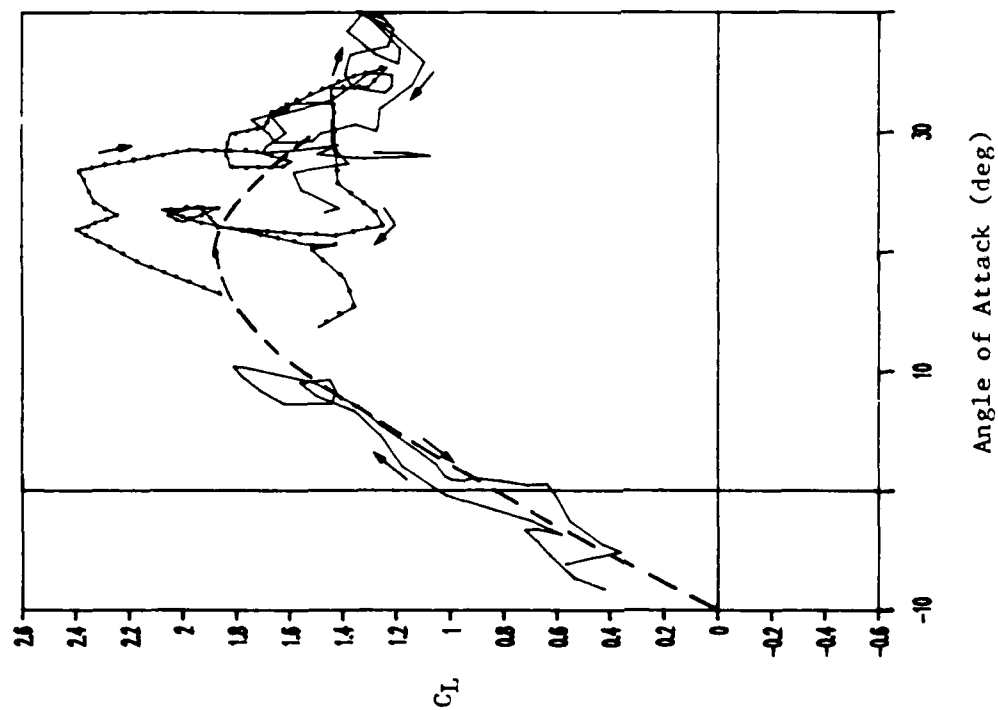


Figure 14. Hysteresis Loops of  $C_L$  for  $\alpha = 3.4^\circ$ ,  $19.9^\circ$  and  $29.3^\circ$ . Series I. The dashed line represents the time-averaged value.

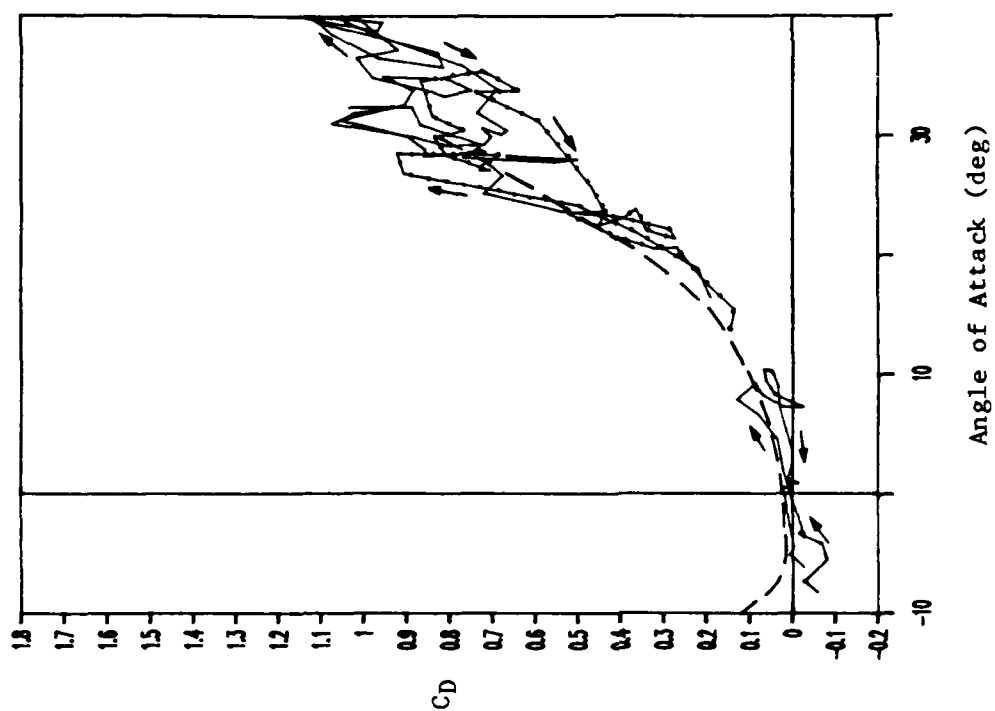


Figure 15. Hysteresis Loops of  $C_D$  for  $\alpha = 3.4^\circ$ ,  $19.9^\circ$  and  $29.3^\circ$ . Series I. The dashed line represents the time-averaged value.

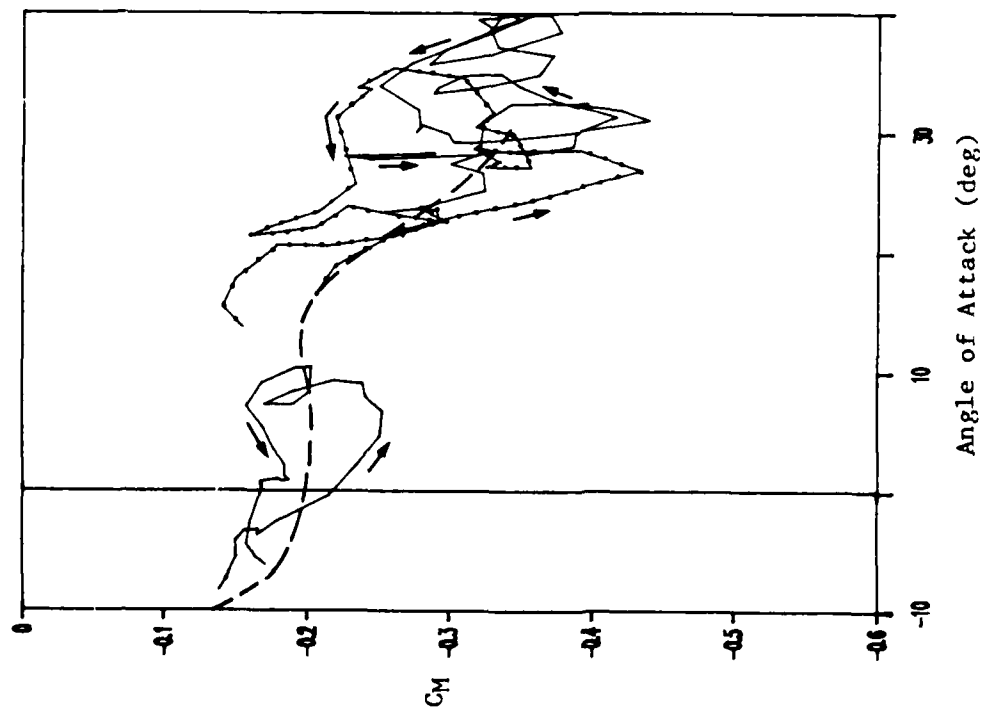


Figure 16. Hysteresis Loops of  $C_M$  for  $\bar{\alpha} = 3.4^\circ$ ,  $19.9^\circ$  and  $29.3^\circ$ . Series I. The dashed line represents the time-averaged value.

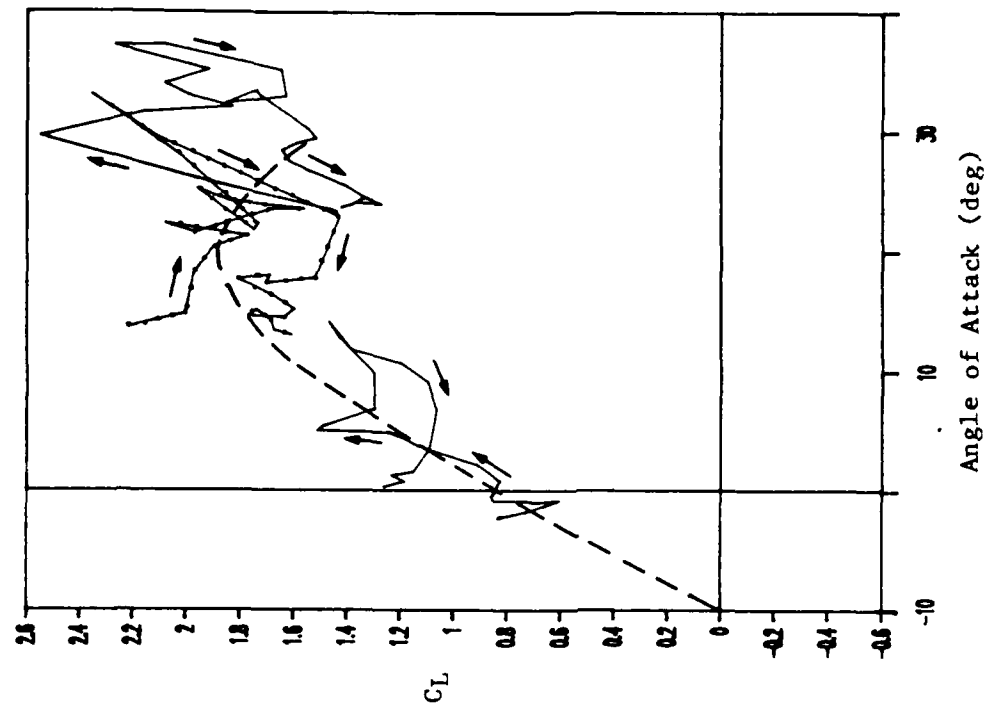


Figure 17. Hysteresis Loops of  $C_L$  for  $\bar{\alpha} = 3.4^\circ$ ,  $19.9^\circ$  and  $29.3^\circ$ . Series II. The dashed line represents the time-averaged value.

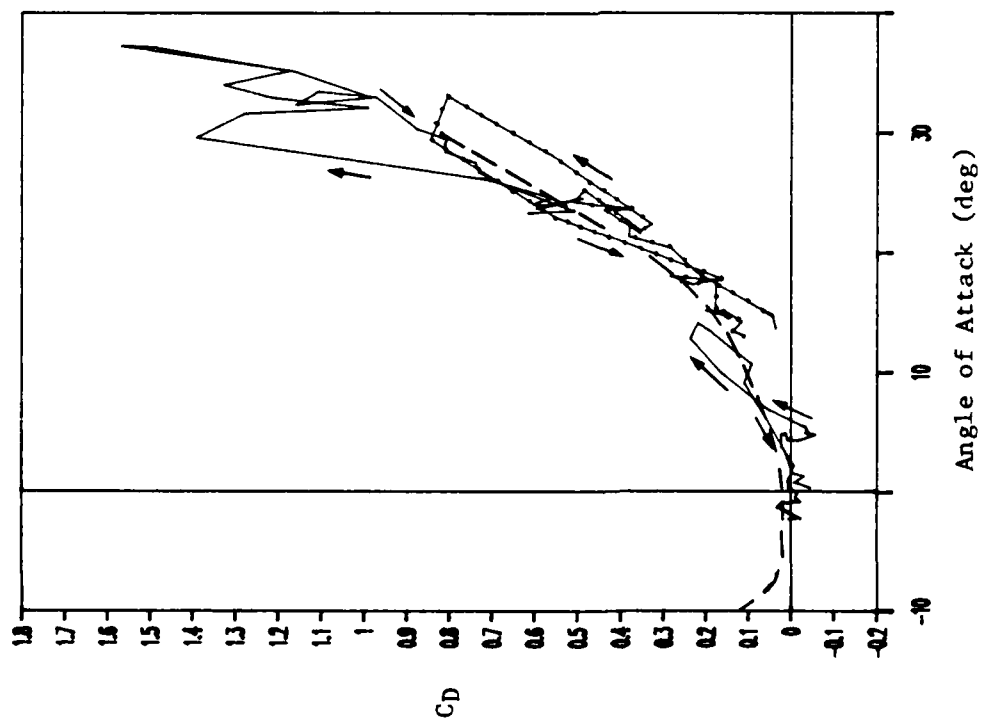


Figure 18. Hysteresis Loops of  $C_p$  for  $\bar{\alpha} = 3.4^\circ$ ,  $19.9^\circ$  and  $29.3^\circ$ . Series II. The dashed line represents the time-averaged value.

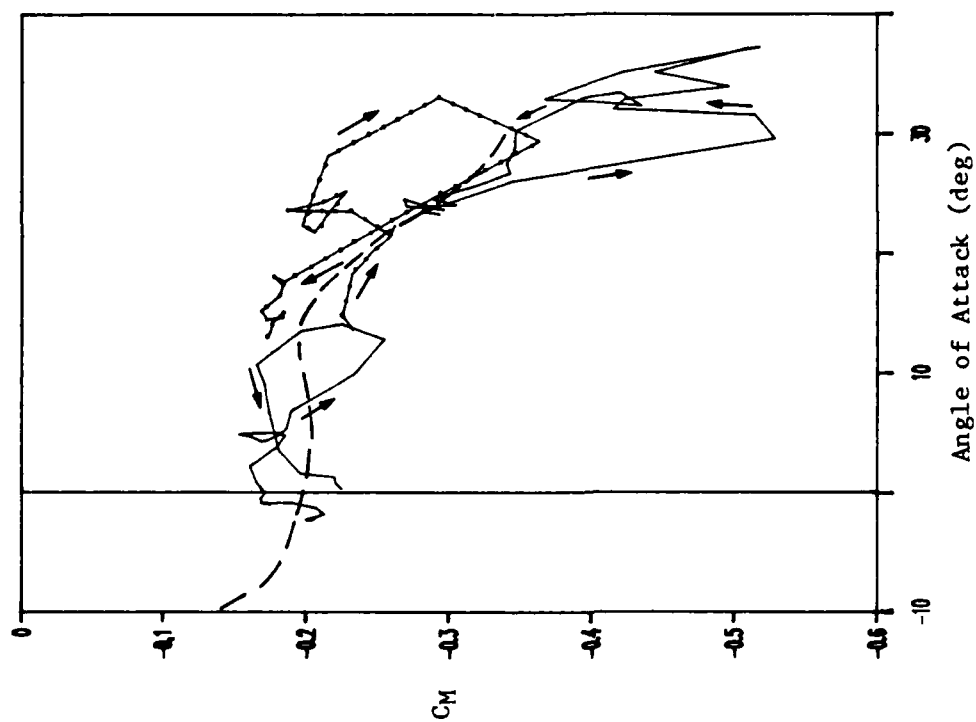


Figure 19. Hysteresis Loops of  $C_m$  for  $\bar{\alpha} = 3.4^\circ$ ,  $19.9^\circ$  and  $29.3^\circ$ . Series II. The dashed line represents the time-averaged value.

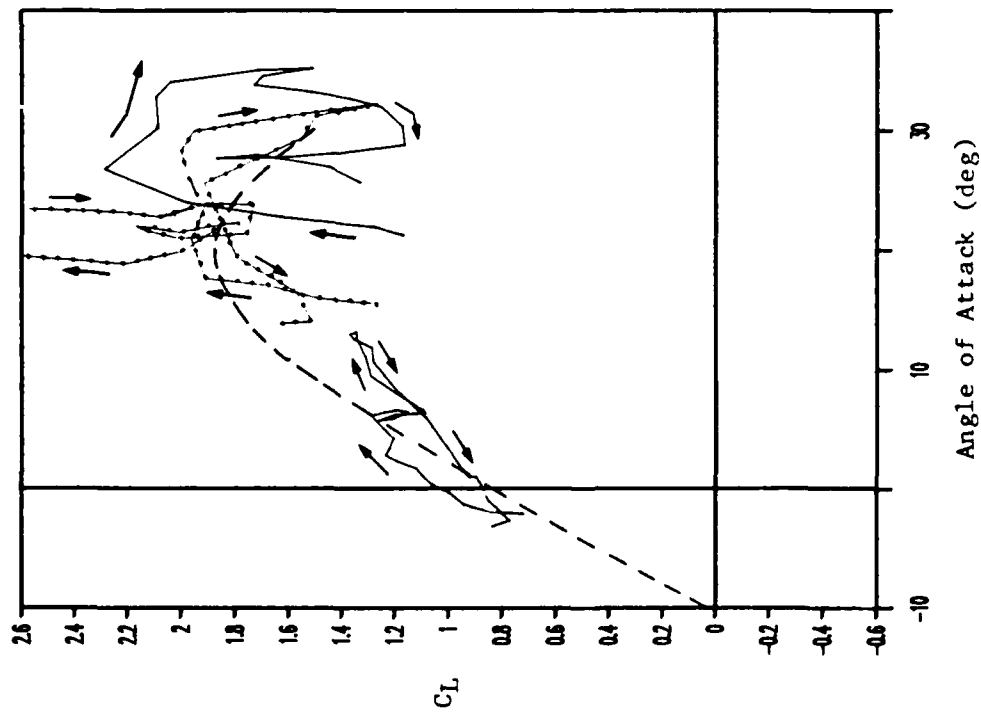


Figure 20. Hysteresis Loops of  $C_L$  for  $\alpha = 3.4^\circ$ , 19.9° and 29.3°. Series III. The dashed line represents the time-averaged value.

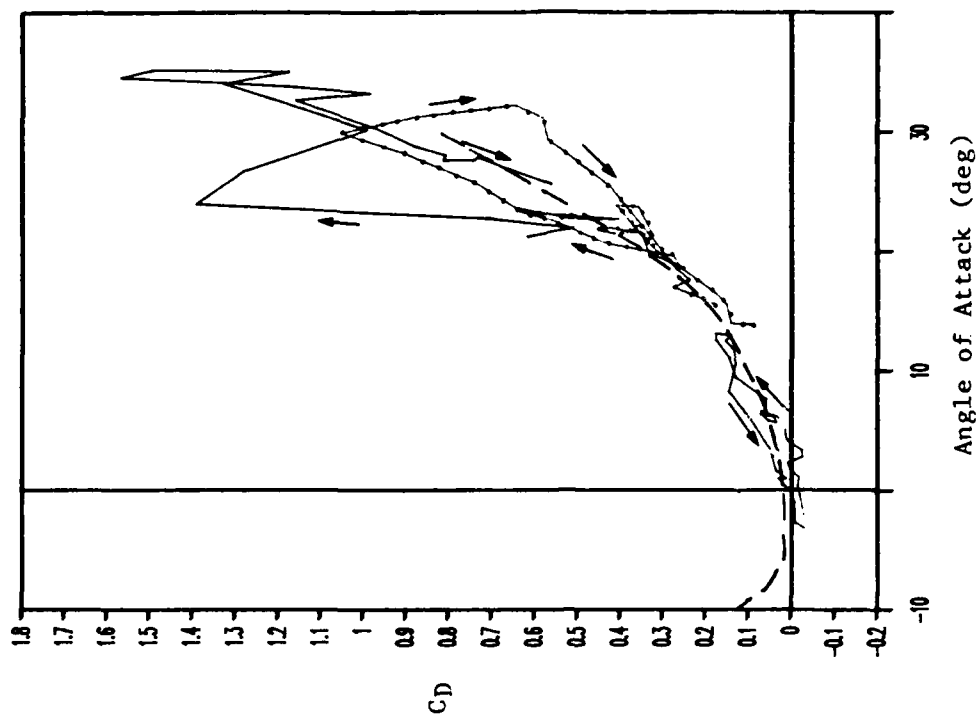


Figure 21. Hysteresis Loops of  $C_D$  for  $\alpha = 3.4^\circ$ , 19.9° and 29.3°. Series III. The dashed line represents the time-averaged value.



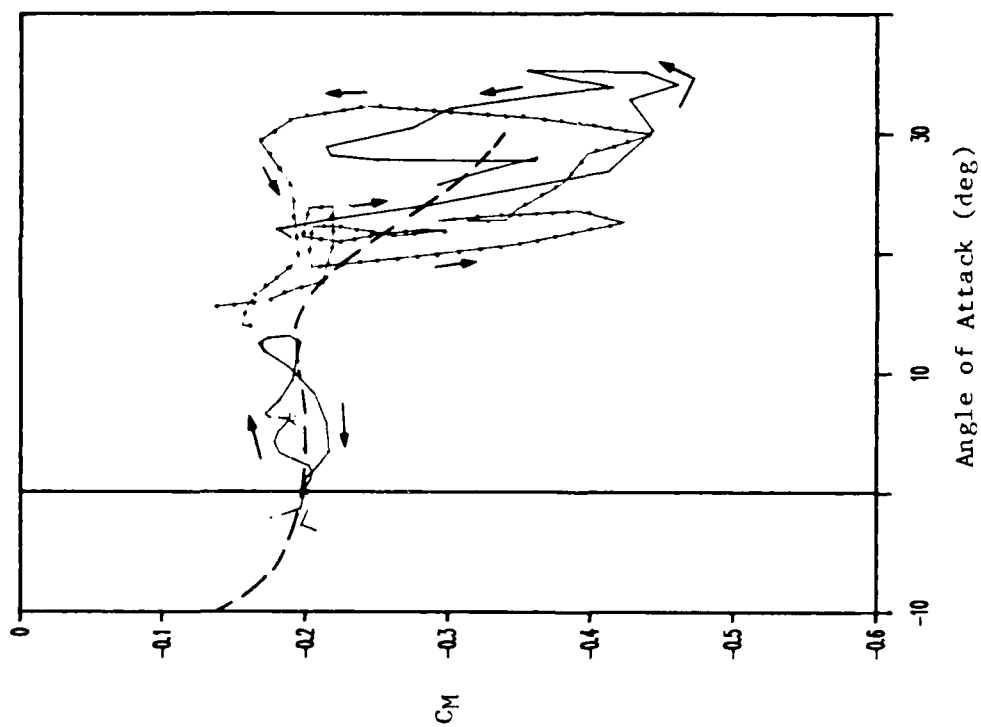


Figure 22. Hysteresis Loops of  $C_M$  for  $\bar{\alpha} = 3.4^\circ$ ,  $19.9^\circ$  and  $29.3^\circ$ . Series III. The dashed line represents the time-averaged value.

simultaneously and that is three-dimensional in nature. All these unsteady components influence the performance of an airfoil (see Reference 8). In addition, the Reynolds number varies within a relatively narrow range. Although complicated, these are the realistic conditions to be encountered by a low-Reynolds-number, low-altitude RPV deployed near the ocean surface. Consequently, we anticipate that the shape of the hysteresis loop will vary significantly in the unsteady but turbulent wind field in comparison with those of the single-frequency oscillating airfoil.

Figures 14, 17 and 20 show three sets of hysteresis loops of  $C_L$  for  $\bar{\alpha} = 3.4^\circ, 19.9^\circ$  and  $29.3^\circ$ . To differentiate the adjacent loops, the one for  $\bar{\alpha} = 19.9^\circ$  is coded with dots. Small arrows are added to direct the time paths of the loops. The loops always start from the end with increasing  $\alpha$  and end with decreasing  $\alpha$ , as directed by the small arrows. The shapes of the loops appear to be vastly different for individual cycles, but they do exhibit some common, organized features. The loops for  $C_L$  at small  $\alpha$  are relatively narrow, similar to those of an oscillating airfoil. The shape is, however, more complicated, with the coexistence of miniloops, and it varies with different cycles. For  $\bar{\alpha} > 19.9^\circ$ , the instantaneous  $C_L$  continues to increase after  $\alpha$  passes the time-averaged DSA (i.e.,  $19^\circ$ ), which is determined from the time-averaged  $C_L$  versus  $\alpha$  curve (Figure 6 in Reference 8). In some cases, the sudden drop in  $C_L$  occurs at a value of  $\alpha$  way beyond  $25^\circ$ . Evidently, there is a time lag between the change in the wind field and the flow field around the wing as it is responding and adjusting to the unsteady wind field. This lag has been observed and documented in laboratory results of an oscillating airfoil.<sup>12,13</sup> Once in a deep stall,  $C_L$  remains low as  $\alpha$  reaches its maximum value and begins to decrease. For the loop with  $\bar{\alpha} = 29.3^\circ$ , the wing is in deep stall most of the time and  $C_L$  may remain low throughout the entire cycle. The lift is usually higher during the first half of the cycle with increasing  $\alpha$  than it is during the second half with decreasing  $\alpha$ . The lift often restores to the neighborhood of the initial value near the end of the cycle as the minimum  $\alpha$  is approached, with some exceptions. The loop for  $\bar{\alpha} = 29.3^\circ$  is very disorganized, which reflects the highly separated flow on the upper surface of the wing in deep stall regime.

Figures 15, 18 and 20 show three sets of hysteresis loops of  $C_D$  for  $\bar{\alpha} = 3.4^\circ, 19.9^\circ$  and  $29.3^\circ$ . Many miniloops are present within the major loops of each individual cycle. Again, the loops for the small  $\alpha$  are relatively

narrow, as expected. The loops for the large angles not only have large amplitudes but also show complex patterns. Each loop deviates significantly from the time-averaged  $C_D$  curve (dashed). For  $\bar{\alpha} = 19.9^\circ$ , there is a sharp rise in  $C_D$  during the increasing  $\alpha$  half of the cycle for all three of the examples. Such a sharp rise corresponds to either an abrupt increase in  $C_L$  or to the shifting into stall onset and light dynamic stall regimes as  $\alpha$  approaches and passes through the DSA. Note that the bulk of  $C_D$  is composed of two components, the coefficients of the form drag and the induced drag; the latter is proportional to  $C_L$ . In the light stall regime,  $C_L$  levels off and begins to drop off, which reduces the contribution of the induced drag to  $C_D$  while the form drag continues to increase. In the deep stall regime,  $C_L$  drops off rapidly and remains low, further reducing the contribution of the induced drag. The form drag increases significantly as a result of the formation of a large separated zone on the upper wing surface, which maintains the increase in  $C_D$  but with a more gentle slope due to reduced contribution from the induced drag.

The hysteresis loops for  $C_M$  are illustrated in Figures 16, 19, and 22. Note that  $C_M$  is negative for a nose-down orientation. Knowing that each loop deviates from others significantly due to the random nature of the cycle, we attempt in the following to describe a general trend of the  $C_M$  loops. Because both  $C_L$  and  $C_D$  contribute to  $C_M$ , the steepest drop or rise of  $C_M$  corresponds to the situation when  $C_L$  and  $C_D$  rise or fall simultaneously. Therefore,  $C_M$  drops abruptly when  $\alpha$  approaches and passes through the DSA before the stall onset, while it rises rapidly when  $\alpha$  has passed the DSA and the wing is experiencing the deep dynamic stall process.  $C_M$  drops again when the wing remains stalled dynamically during which  $C_L$  is low and  $C_D$  rises due to the increase in the form drag. Finally,  $C_M$  rises and returns to roughly the initial value at the end of the cycle as  $\alpha$  passes the maximum angle during that cycle and begins to decrease again. For a cycle with an amplitude of  $5^\circ$  to  $6^\circ$ , the excursion of  $C_M$  could be 0.2 or larger for  $\bar{\alpha} = 19.9^\circ$  and  $29.3^\circ$ .

Of all the  $C_M$  loops, only the one for  $\bar{\alpha} = 19.9^\circ$  shows a negative damping loop (clockwise). At that angle, the wing is in and out of dynamic stall, a favorable condition for negative damping. During that cycle, the area of the clockwise loop is considerably larger than that of the counterclockwise loop. Under this condition, the wing could experience stall flutter provided its structural natural frequency is close to the dominant frequency of the wind field.

### Frequency Spectra of Ambient and Aerodynamic Parameters

The frequency spectra of  $U$ ,  $W$ ,  $\alpha$ ,  $L$ ,  $D$  and  $M$  for four runs with  $\bar{\alpha} = 3.4^\circ$  (rectangles),  $19.9^\circ$  (pluses),  $23.0^\circ$  (diamonds) and  $29.3^\circ$  (triangles) are shown in Figures 23 through 28. The spectra were estimated by calculating the power spectra of the individual time series averaged over 0.1 second. There were a total of 900 data points. First, we removed the linear trend from the time series and then added 62 zeros to each end of the time series to make up a total of 1024 points for evaluating the power spectra. A cosine window as described by Bendat and Piersol<sup>22</sup> was used to reduce leakage outside the frequency band  $f = \pm 1/T$ , where  $T$  is the total time or 102.3 seconds. The power spectra were evaluated by using the algorithm available in the ASYSTANT scientific software (Macmillan Software Company) for IBM PC/AT or compatibles. To reduce the spread of the spectral density, a running mean algorithm was applied by averaging one to nine points of the frequency distribution, with gradual increase in the number of points from the low- to high-frequency end.

The spectra of the  $U$  and  $W$  wind components for the four runs (Figures 23 and 24) show that the shapes of the spectra are quite similar. The difference in the spectral density is mainly due to the variations in the turbulence intensity of the individual runs, as anticipated. From Table 1, we determined that the turbulence intensities  $u'/\bar{U}$  for the four runs are 0.12, 0.16, 0.13 and 0.12, respectively. Figures 23 and 24 show that the amplitude of the spectral density is, on the average, proportional to  $u'/\bar{U}$ . The same characteristics are observed for the spectra of  $\alpha$  (Figure 25), which are, of course, closely related to those of  $U$  and  $W$ . The  $U$  spectra show a  $-5/3$  slope for about one decade up to  $f \approx 1$  to 2 Hz. Beyond 2 Hz, the spectral density rolls off at a slope slightly steeper than  $-5/3$ . As discussed in Liu,<sup>8</sup> the steep rolloff is due to an insufficient frequency response of the Gill propeller anemometer whose  $-3$  dB points is about 2 Hz at  $\bar{U} = 8$  m/s. The  $W$  spectra (Figure 24) show a slightly narrower  $-5/3$  region than the  $U$  spectra. Beyond 2 Hz, the rolloff is slightly steeper for the  $W$  spectra than for the  $U$  spectra. Again, as discussed by Liu,<sup>8</sup> the response in the  $W$  component of the Gill propeller is worse due to the small value of  $\bar{W}$ . A partial remedy was made by tilting the anemometer at an angle of  $15^\circ$  to improve the frequency response of  $W$ . The  $\alpha$  spectra show a shape similar to that of the  $W$  spectra, because  $\alpha = \arctan(W/U)$ .

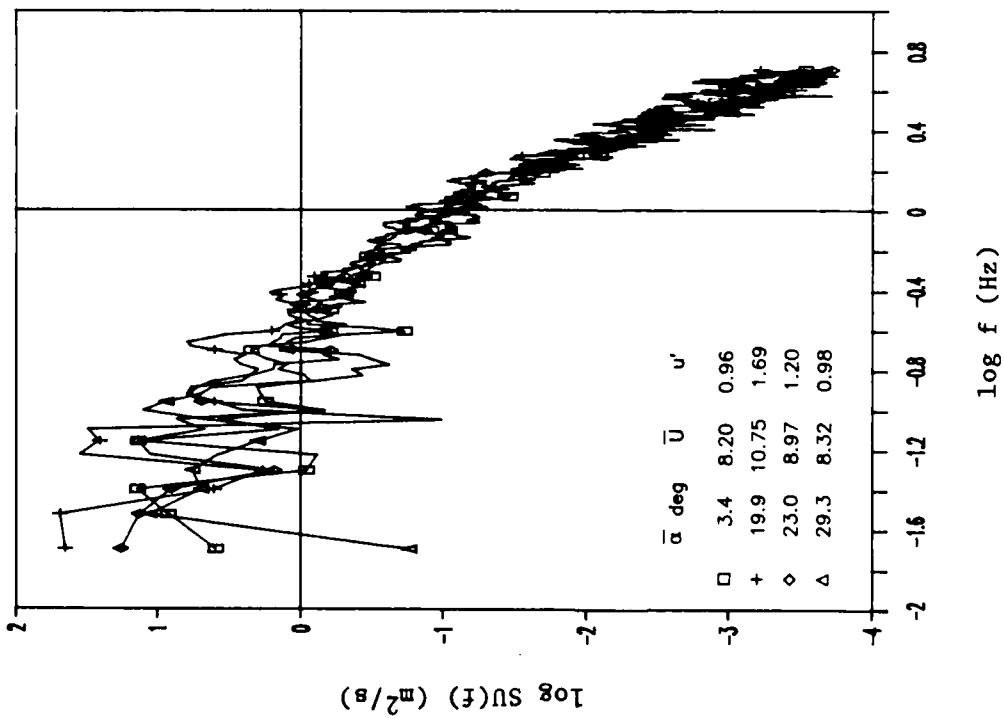


Figure 23. Spectra of the U Component for Four Selected Runs.

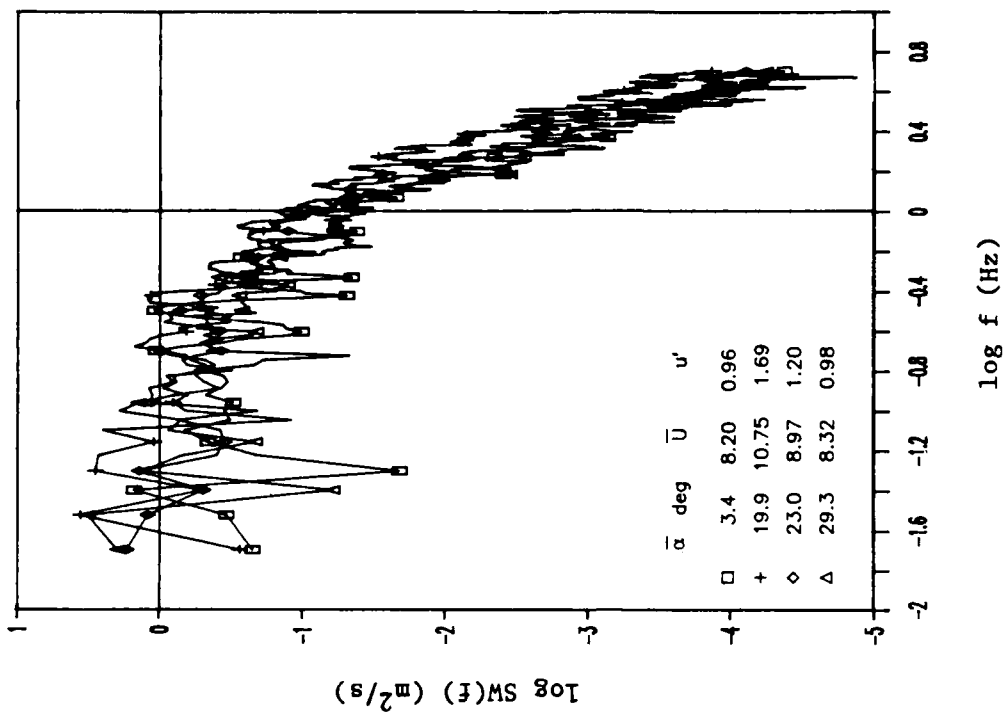


Figure 24. Spectra of the W Component for Four Selected Runs.

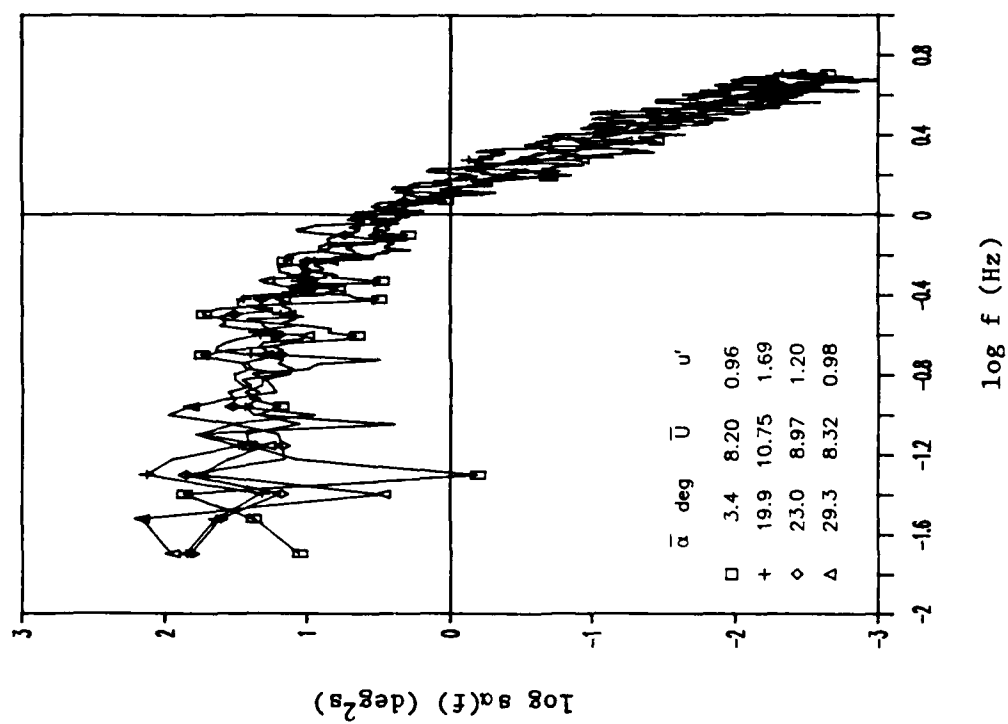


Figure 25. Spectra of the Angle of Attack for Four Selected Runs.

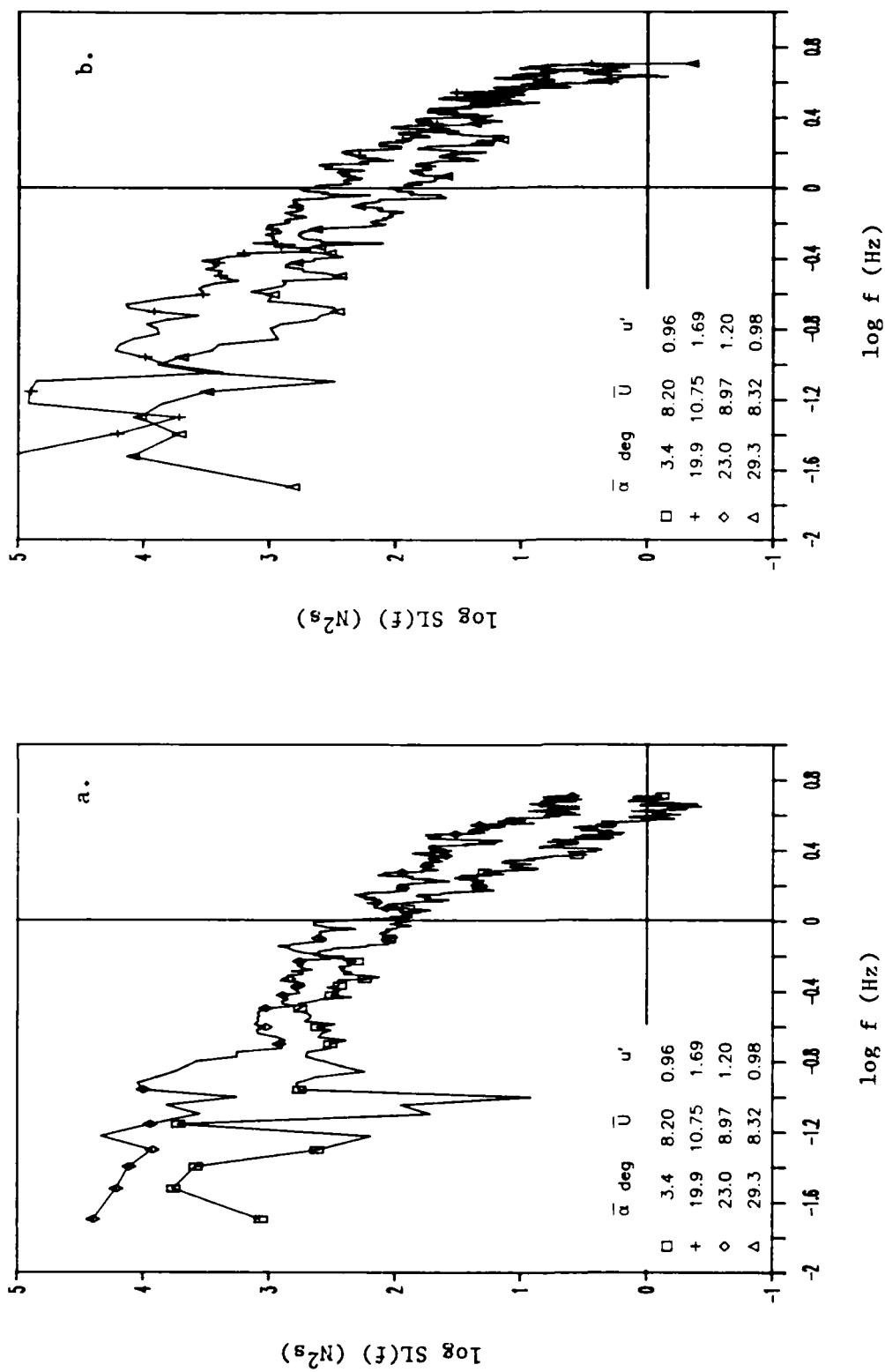


Figure 26. Spectra of the Lift for Four Flow Regimes: No Stall, Stall Onset, Light Stall, and Deep Dynamic Stall.

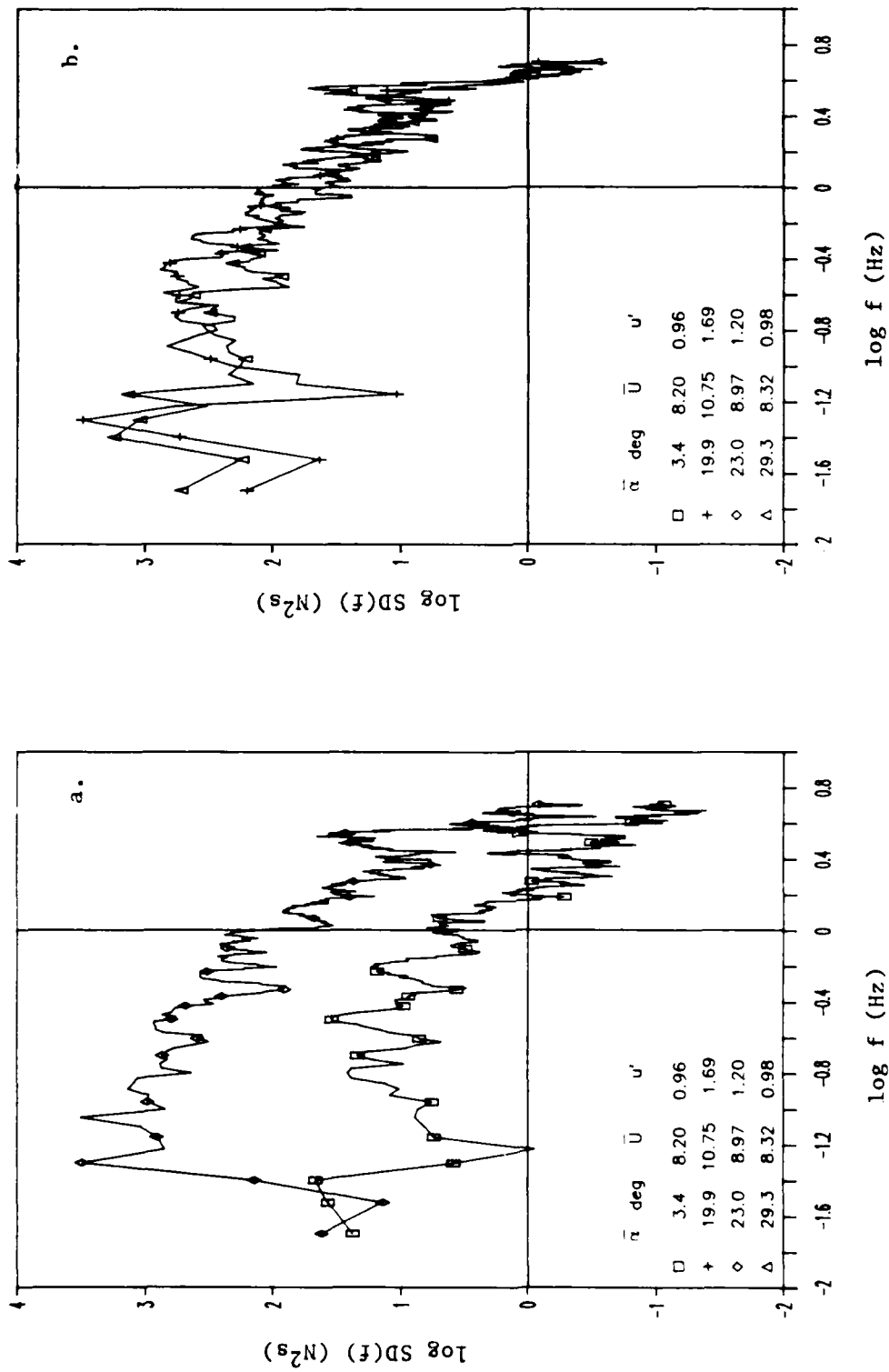


Figure 27. Spectra of the Drag for Four Flow Regimes: No Stall, Stall Onset, Light Stall, and Deep Dynamic Stall.



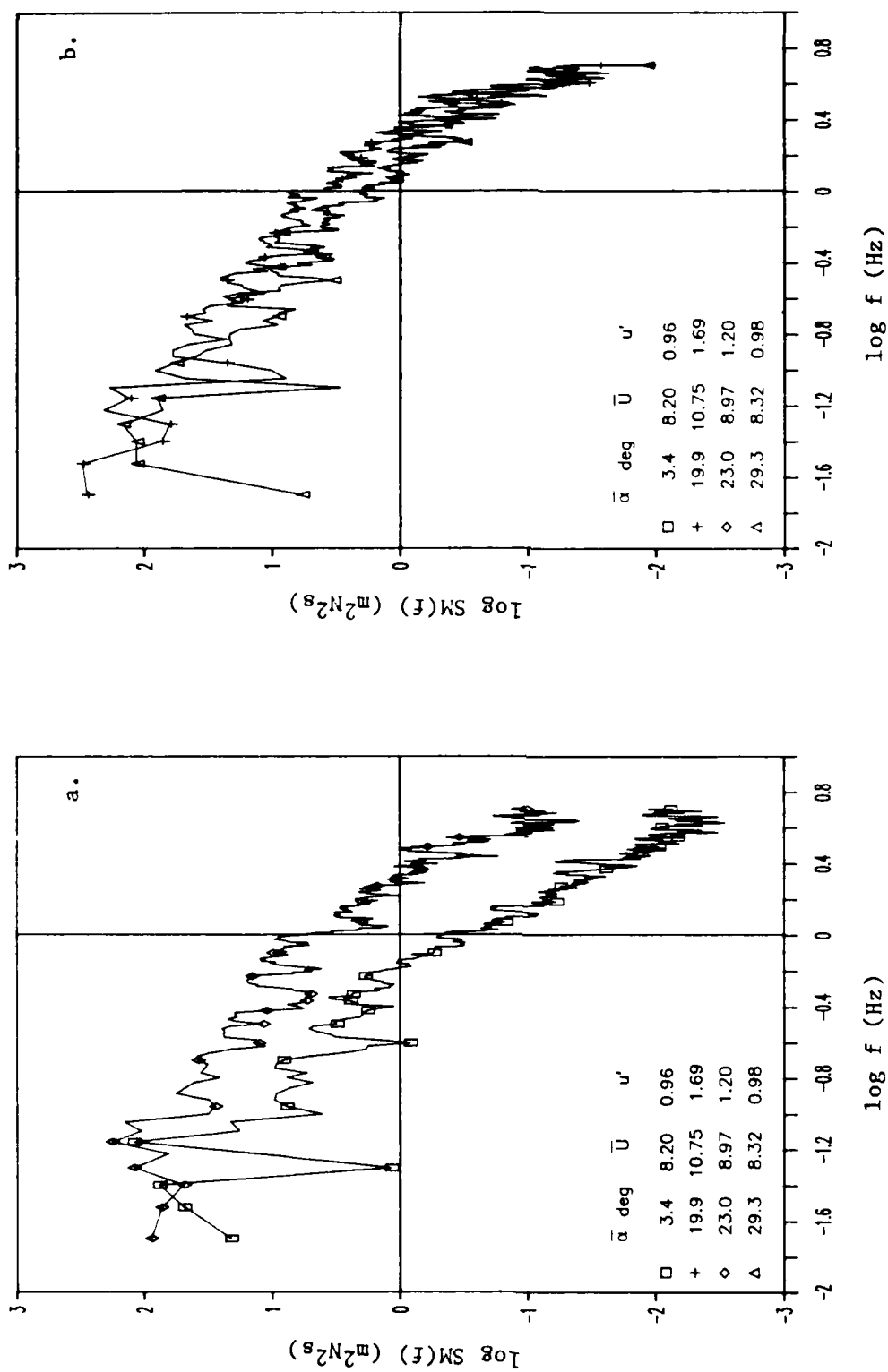


Figure 28. Spectra of the Pitching Moment for Four Flow Regimes: No Stall, Stall Onset, Light Stall, and Deep Dynamic Stall.

The L, D and M spectra (Figures 26 through 28) all display a region of  $-5/3$  slope up to 4 Hz, which is higher than those of the U and W spectra. As described by Liu,<sup>8</sup> the frequency response of the aerodynamic balance was significantly higher than that of the Gill anemometers. To match the frequency response of the two instruments, the outputs of the aerodynamic balance were low-pass filtered at 4 to 5 Hz ( $-3$  dB). This matching was essential to avoid artificial spikes in the spectra of  $C_L$ ,  $C_D$  and  $C_M$  due to the above mismatch, as the coefficients were derived from simultaneous measurements of the wind and force components. It should be pointed out that the L, D and M spectra depend on the variations in U and W or  $\alpha$ . Attempts will be made to isolate the dependence of these parameters by correcting the spectra with the turbulence intensity. Without the correction, the effects of dynamic stall on the spectra cannot be assessed due to the interdependence of the spectra on U and  $\alpha$ . In particular, the L spectra (Figure 26) tend to be a stronger function of U than of  $\alpha$ . The effects of the dynamic stall on the L spectra are therefore masked by those of U. The D and M spectra (Figures 27 and 28), on the other hand, show a stronger dependence on  $\alpha$  than on U. For example, the spectral densities for  $\bar{\alpha} = 3.4^\circ$  (rectangles) are significantly lower than those for  $\bar{\alpha} = 19.9^\circ$ ,  $23.0^\circ$  and  $29.3^\circ$ . For  $\bar{\alpha} > 19^\circ$ , however, the effects of the dynamic stall again cannot be isolated from those of U. Note that there are two distinct spikes at  $f \approx 2.7$  and  $3.5$  Hz in the D spectra for  $\bar{\alpha} = 3.4^\circ$ . The spikes persist, but the frequencies shift slightly for the large angles. No such spikes are present in either the L or M spectra.

To isolate the dependence of  $\alpha$  from that of U, we corrected the U, W and  $\alpha$  spectra by dividing them with the square of the turbulence intensity or  $u'^2/\bar{U}^2$ . Such a correcting factor was selected based on the physically consistent relation  $\int \phi_U(f) df = u'^2$  where  $\phi_U$  is the spectral density of U. Figures 29 through 31 illustrate the corrected U, W and  $\alpha$  spectra. It is evident that the correction has collapsed the spectra and has reduced the dependence of U significantly. Similarly, we corrected the L, D and M spectral densities by dividing them with the  $u'/\bar{U}$ , which is again physically consistent because  $L \propto U^2$ . Figures 32 through 34 illustrate the corrected L, D and M spectra.

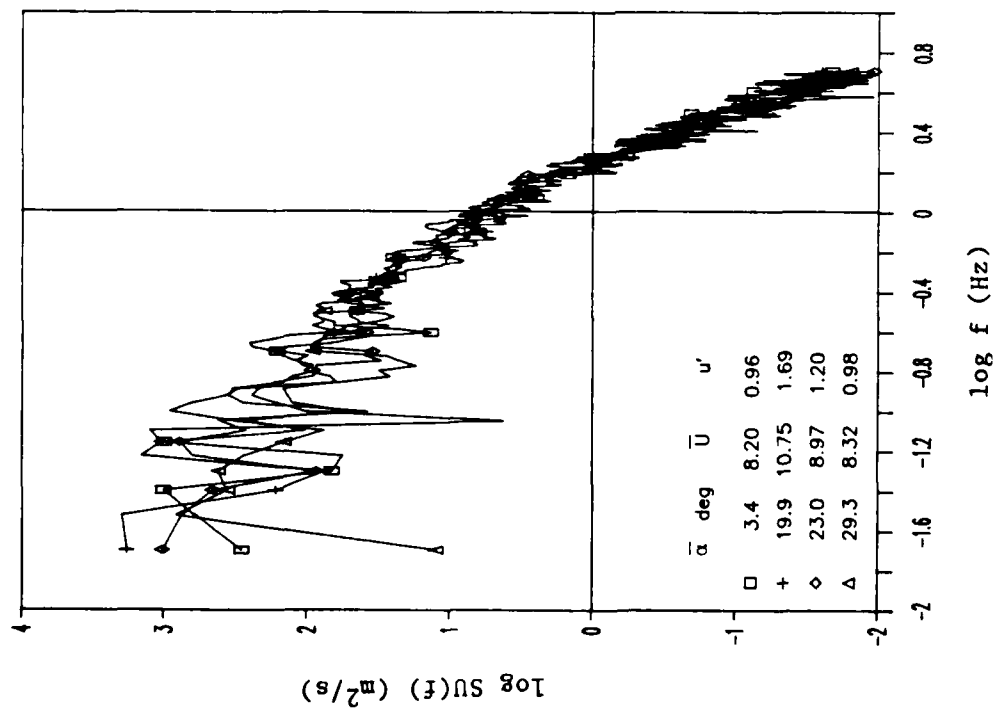


Figure 29. Corrected Spectra of the U Component for Four Selected Runs.

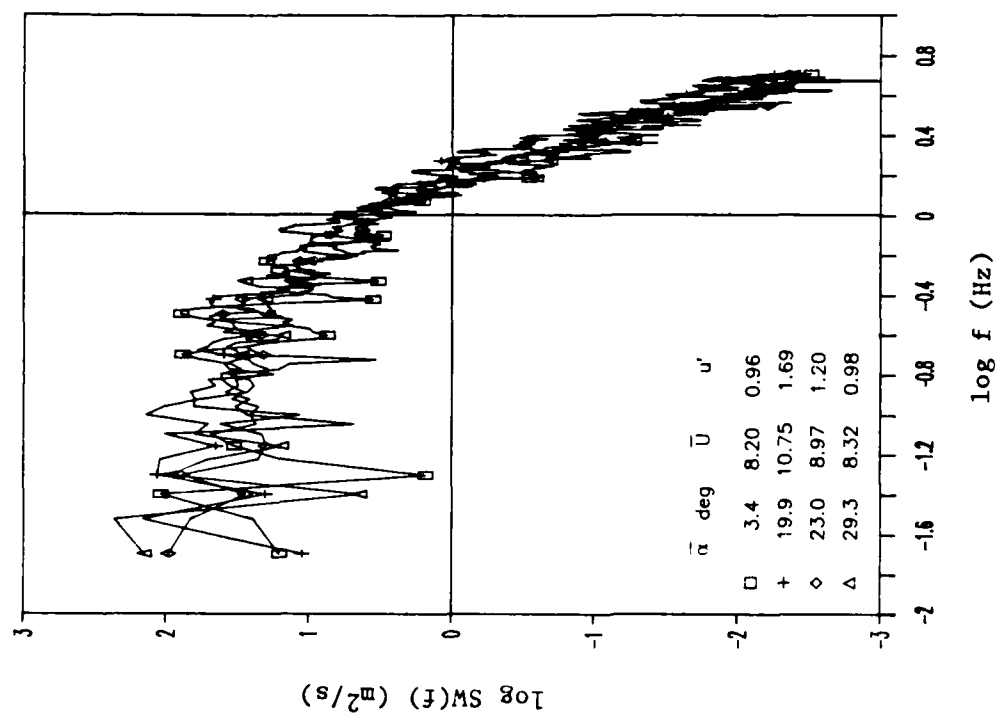


Figure 30. Corrected Spectra of the W Component for Four Selected Runs.

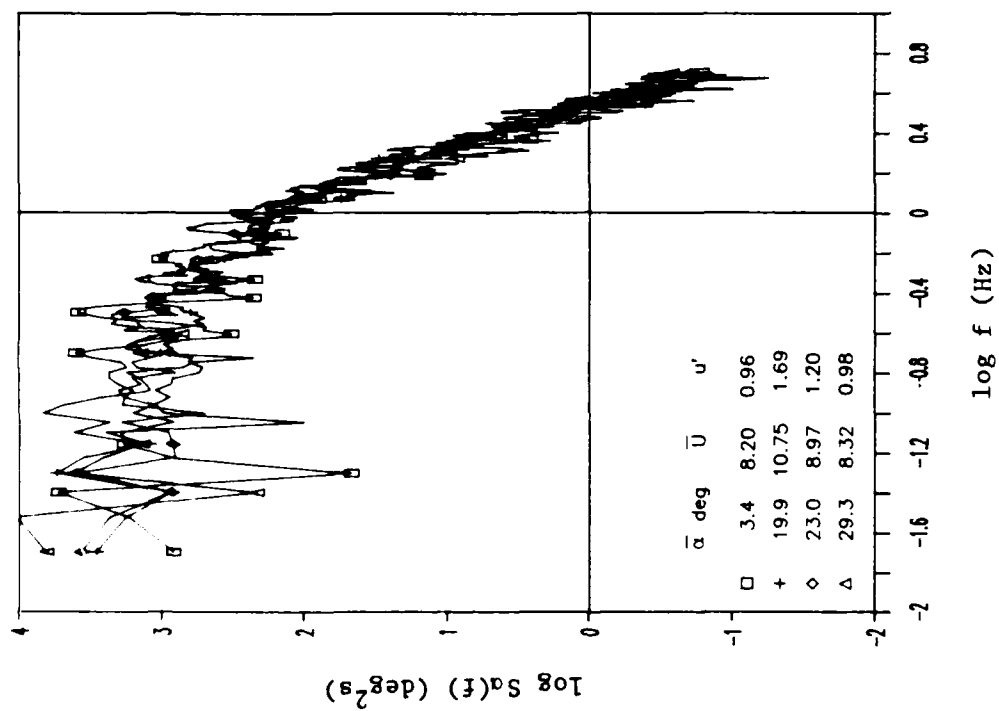


Figure 31. Corrected Spectra of the Angle of Attack for Four Selected Runs.

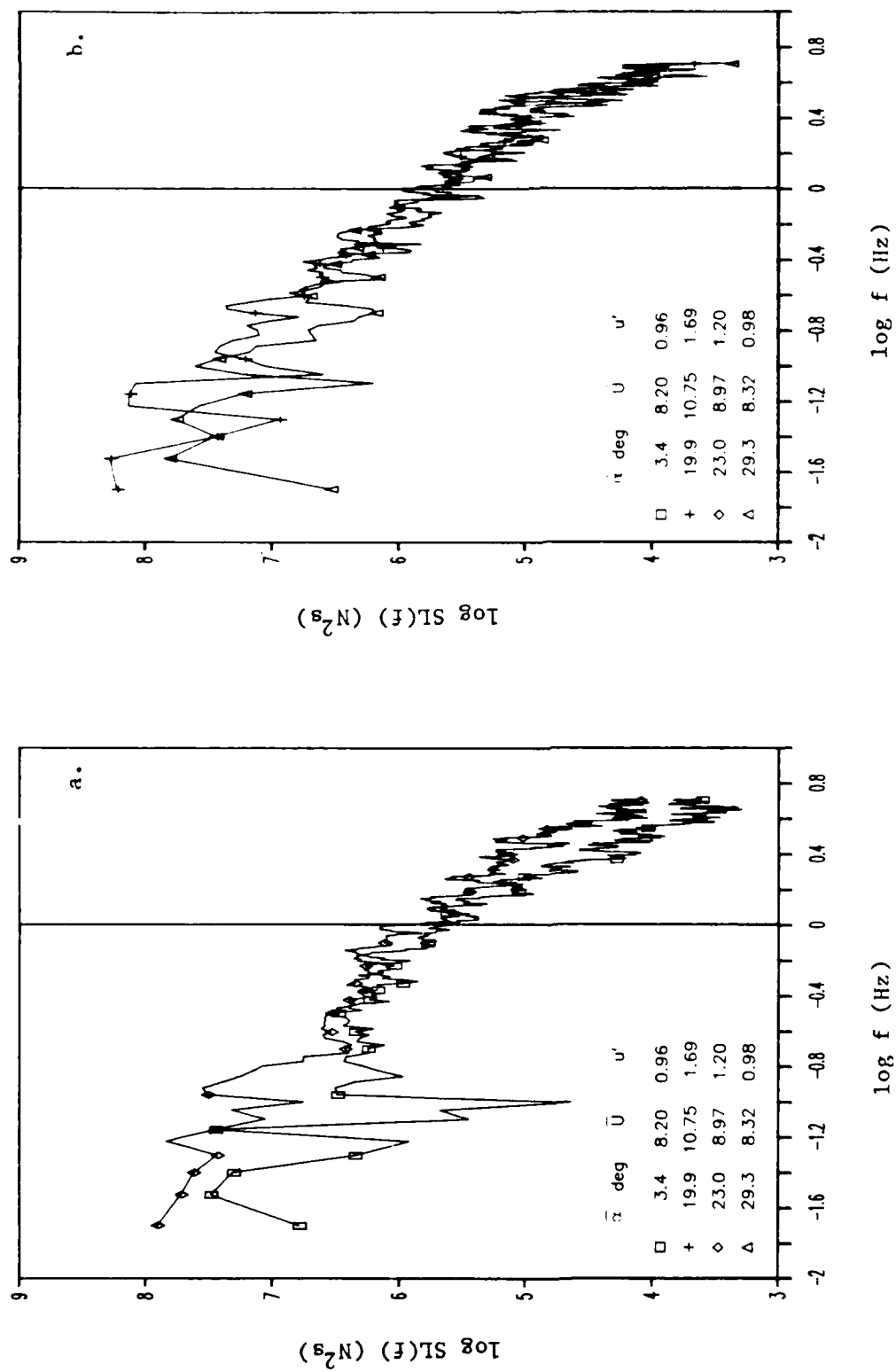


Figure 32. Corrected Spectra of the Lift for Four Flow Regimes: No Stall, Stall Onset, Light Stall, and Deep Dynamic Stall.

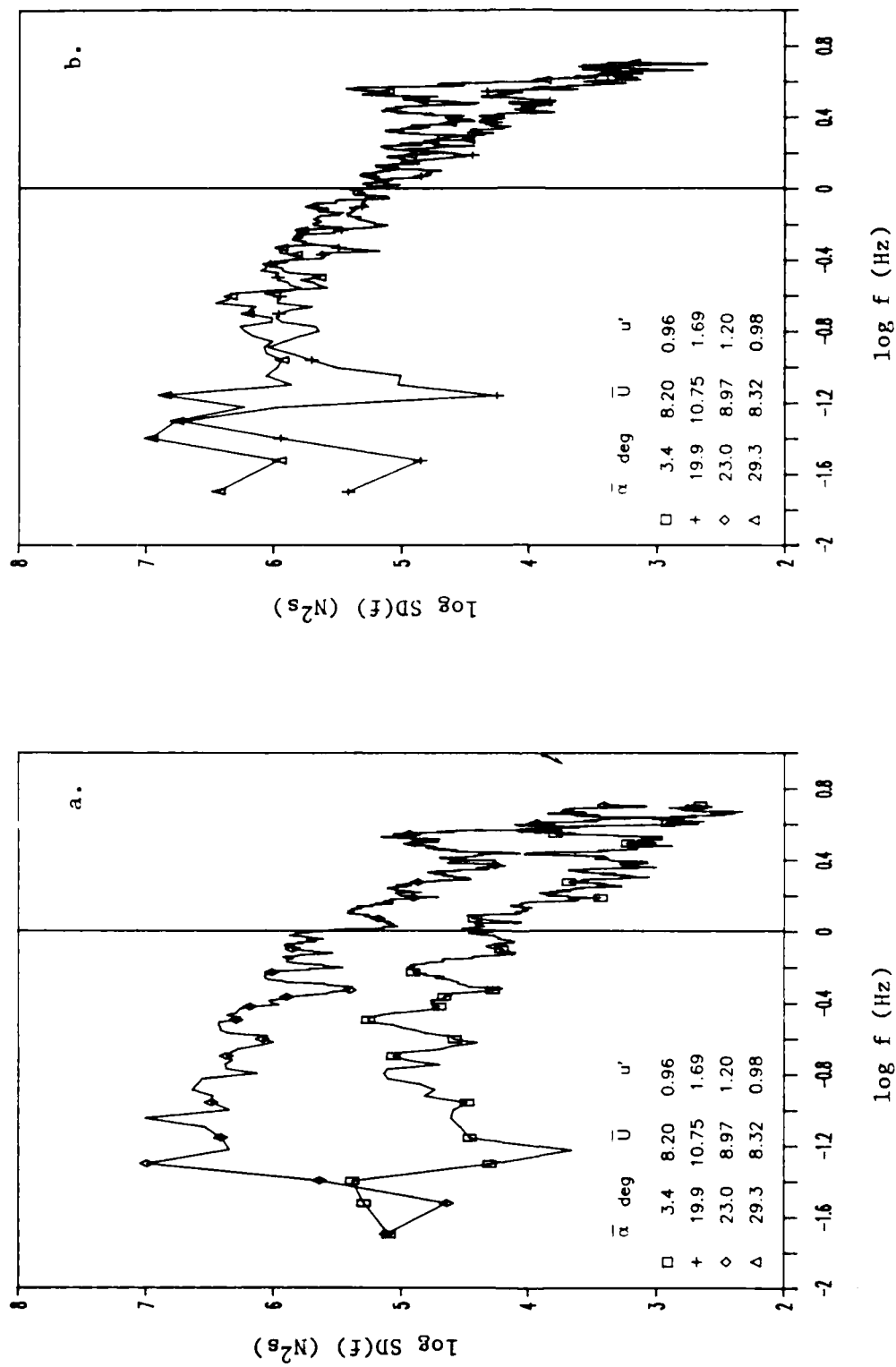


Figure 33. Corrected Spectra of the Drag for Four Flow Regimes: No Stall, Stall Onset, Light Stall, and Deep Dynamic Stall.

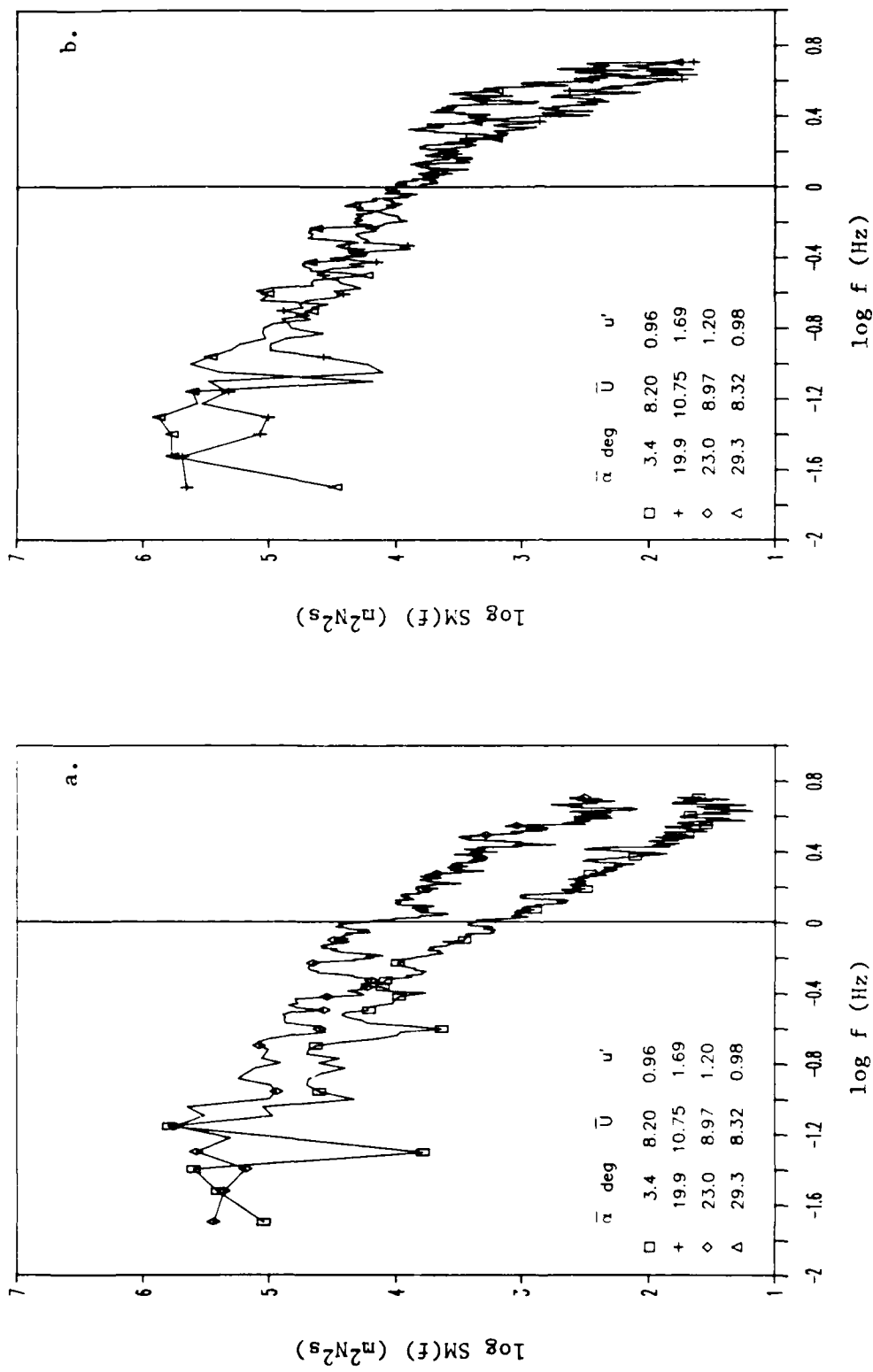


Figure 34. Corrected Spectra of the Pitching Moment for Four Flow Regimes: No Stall, Stall Onset, Light Stall, and Deep Dynamic Stall.

From the corrected L spectra (Figure 31), we observe that the spectral densities for  $\bar{\alpha} = 3.4^\circ$  is generally lower at low ( $f < 0.3$  Hz) and high ( $f > 0.3$  Hz) frequencies than those for  $\bar{\alpha} = 23.0^\circ$  and  $29.3^\circ$ . They become roughly the same for medium frequencies ( $0.3 \text{ Hz} < f < 1.3 \text{ Hz}$ ). This reflects the presence of low- and high-frequency fluctuations beyond the stall onset angles for L, D and M. Note that the runs for  $\bar{\alpha} = 23.0^\circ$  and  $29.3^\circ$  correspond to the wing in the light and deep dynamic stall regimes, respectively, most of the time. For  $\bar{\alpha} = 19.9^\circ$ , with the wing operating constantly in and out of dynamic stall (stall onset), the spectral densities are the highest at low frequencies ( $f < 0.4$  Hz). For  $f > 0.4$  Hz, the spectral densities are inbetween those for  $\bar{\alpha} = 3.4^\circ$  and  $23.0^\circ$ . The above observations indicate that the L spectra are generally low for all but the medium frequencies. In the vicinity of stall onset, the L spectral densities increase the most at low frequencies, whereas light and deep stall promote high-frequency fluctuations in the presence of highly separated flows on the upper wing surface.

The corrected D spectra (Figure 33) show more dramatic differences. For  $\bar{\alpha} = 3.4^\circ$ , the spectral density is consistently lower than those of the others for all frequencies. The presence of two distinct spikes at  $f = 2.7$  and  $3.6$  Hz is evident, but their source is not known at present. For  $\bar{\alpha} = 19.9^\circ$ , the spectral density is significantly higher than that for  $\bar{\alpha} = 3.4^\circ$  but consistently lower than those for  $\bar{\alpha} = 23.0^\circ$  and  $29.3^\circ$ . The spectral densities for  $\bar{\alpha} = 23.0^\circ$  and  $29.3^\circ$  are quite similar; the latter is higher with more distinct spikes at high frequencies. This is consistent with the finding that the hysteresis loops have relatively large excursions as the wing is operating in and out of the deep dynamic stall regime. Furthermore, we anticipate that the flow for  $\bar{\alpha} = 23.0^\circ$  is not as strongly separated as that for  $\bar{\alpha} = 29.3^\circ$ , as  $C_L$  drops off and remains low whereas  $C_D$  continues to rise when  $\bar{\alpha}$  increases from  $23.0^\circ$  to  $29.3^\circ$ .

The corrected M spectra (Figure 34) have shapes between those of the L and D spectra because both L and D contribute to form M. One of the most distinct differences in the M spectra is that, for  $\bar{\alpha} = 3.4^\circ$ , they have a slope considerably steeper than those of the rest (roughly  $-5/3$  slope). The two distinct spikes at  $f = 2.7$  and  $3.6$  Hz, as observed in the D spectra, are no longer present in the M spectra. At the high-frequency end, the spectra for  $\bar{\alpha} = 29.3^\circ$  have the highest spectral density, followed sequentially by those for  $\bar{\alpha} = 23.0^\circ$ ,  $19.9^\circ$  and  $3.4^\circ$ .



Comparison of the L, D and M spectra indicates that the unsteady wind field has the most impact on D followed by M and has the least impact on L, as far as the high-frequency components are concerned. The dynamic stall has significant effects on these spectra at frequency greater than about 2 Hz where noticeable increase in the spectral density is observed. When the wing is going through light and deep dynamic stall, especially the latter, the spectra becomes spiky with relatively well-defined dominant frequencies. The spiky spectra are a signature of the presence of large hysteresis loops.

#### 4. SUMMARY

An environmental aerodynamic test system (EATS) was designed and assembled to investigate the effects of atmospheric unsteadiness (turbulence and gust) on the performance of a full-scale Wortmann FX-63-137 wing (smoothed by Eppler) (see Section 2 and also References 8 and 16). Several series of experiments were conducted under a "park-mode" configuration by directing the wing into the prevailing wind at windy sites (see Section 3 and Reference 8). The time-averaged aerodynamic parameters derived from the full-scale experiments differ considerably from those of the wind tunnel counterparts under steady conditions. The unsteady wind field was demonstrated to have significantly favorable effects on the performance of the Wortmann wing.<sup>8</sup> The most important unsteady effects pertain to the lift overshoot, stall delay, reduction of drag and endurance enhancement. The lift overshoot and stall delay are consistent with wind tunnel observations for an oscillating airfoil.<sup>10</sup>

To understand the above unsteady effects, further analysis of the full-scale data was conducted with emphasis on examining the time series, the unsteady loops and the frequency spectra of the ambient and aerodynamic parameters. The salient points derived from the analysis are summarized below.

- (1) For small  $\bar{\alpha} \approx 3.4^\circ$ , which is in the minimum drag regime, the time series of  $D$  shows instantaneous negative values (i.e., propulsion), although the time-averaged drag is positive.<sup>8</sup> The exact mechanism that generates the instantaneous propulsion is not known.
- (2) For large  $\alpha$  in the neighborhood of the dynamic stall angle, the time series of  $L$ ,  $D$  and  $M$  contain some spikes with large fluctuations. The unsteady wind field changes the instantaneous angle of attack of the Wortmann wing and causes it to experience the dynamic stall phenomenon, which is drastically different from the static stall phenomenon. During any one of the random cycles with a sufficiently large-amplitude fluctuation in the  $W$  component, the wing, which is initially not stalled, may go through all the dynamic stall regimes (stall onset, light and deep stall):
  - o Before stall onset, significant lift overshoot was observed, resulting in a large increase in  $C_L$  (from 1.6 to over 2.0). The instantaneous stall onset takes place after  $\alpha$  greatly exceeds the time-averaged dynamic stall angle (about  $19^\circ$ ).<sup>8</sup> This stall

delay is due to the time lag for the adjustment of the unsteady flow field around the wing in response to the change of the wind field (Figures 14 through 22). The lift overshoot leads to a considerable increase in the drag due to the increase in both the form and induced drag. The pitching moment begins to drop off sharply as the lift overshoots its maximum static value.

- o At stall onset, the lift levels off and drops slightly. The pitching moment shows similar behavior. The drag appears to rise continuously due to the increase in the form drag, although the contribution of the induced drag decreases.
- o Further increase in  $\alpha$  causes the wing to enter the light stall regime with the lift dropping off, the pitching moment rising and the drag dropping off momentarily.
- o Negative aerodynamic damping is experienced by the wing as it is in and out of stall. Stall flutter may be initiated provided the natural structural frequency of the wing is close to the dominant frequency of the wind field.
- o As the wing enters the deep stall regime, the lift drops below the maximum time-averaged value. During that time, the thickness of the separation region increases to the scale of the chord. As a result, the form drag rises sharply. The total drag rises more moderately due to the decrease in the induced drag. Meanwhile, the pitching moment drops to its minimum value.
- o As  $\alpha$  reaches its maximum and begins to decrease, the lift, drag and pitching moment begin their recovery. At the end of the cycle, they restore to roughly the initial values. The paths during the two halves of the cycle differ significantly, which forms the hysteresis loops. Due to the randomness of the wind field, the hysteresis loops consist of many miniloops and are much more complicated than those of an oscillating airfoil with a single frequency. The dynamic stall process is presented in terms of the response in the forces and moment as can be seen in both the time series and the unsteady loops (Figures 2 through 22.)

(3) The frequency spectra of the ambient parameters demonstrate that the spectral shapes are similar for the four runs selected for detailed investigation, i.e., with  $\bar{\alpha} = 3.4^\circ, 19.9^\circ, 23.0^\circ$  and  $29.3^\circ$ . The spectral densities for U, W and  $\alpha$  are proportional to U and  $\alpha$ . The spectra collapse reasonably well when they are corrected for by dividing the square of the turbulence intensity or  $u'^2/\bar{U}^2$ . Such physically consistent correction effectively removes the dependence of the spectra on U. Similarly, the spectra of the aerodynamic parameters are corrected for by dividing  $u'/\bar{U}$  to remove their dependence on U. Comparison of the corrected spectra of the aerodynamic parameters has shown several important features:

- o The unsteady wind field has the most impact on the drag spectra followed in order by the pitching moment and lift spectra. For example, the spectral density of the drag for  $\bar{\alpha} = 3.4^\circ$  is consistently 1 to 2.5 orders lower than that for  $\bar{\alpha} = 23.0^\circ$  or  $29.3^\circ$ , except at the low-frequency end where the resolution of the spectral analysis is less adequate. The spectral density of the pitching moment is over 1 order of magnitude lower for  $\bar{\alpha} = 3.4^\circ$  than for  $\bar{\alpha} = 23.0^\circ$  or  $29.3^\circ$  for frequencies higher than 1 Hz. The shapes of the L and M spectra show a steeper slope at the high-frequency end for  $\bar{\alpha} = 3.4^\circ$  than for its high  $\alpha$  counterparts, especially for the L spectra.
- o As a result of dynamic stall, the spectral densities of L, D and M at high frequencies increase considerably together with the introduction of large-amplitude spikes with well-defined dominant frequencies. The spikes, especially in the D spectra, are most distinctive for  $\bar{\alpha} = 29.3^\circ$  when the wing is in the deep stall regime most of the time. The distinct spikes are the signatures of the presence of large hysteresis loops.

## REFERENCES

1. Office of Naval Research (1983) "Workshop on Low-Reynolds-Number Aerodynamics," Office of Naval Research, Arlington, VA, February.
2. Carmichael, B. H. (1981) "Low Reynolds Number Airfoil Survey," Vol. 1, NASA CR165803.
3. Lissaman, P. B. S. (1983) "Low-Reynolds-Number Airfoils," Ann. Rev. Fluid Mech., Vol. 15, pp. 223-39.
4. Mueller, T. J. (1985) "Low Reynolds Number Vehicles," AGARDograph No. 288, February, 69 pp.
5. Lieback, R. H. (1986) "Low Reynolds Number Airfoil Design at the Douglas Aircraft Company," Proc. of the Conf. on Aerodynamics at Low Reynolds Numbers, Royal Aeronautical Society, London, Britain, October, Vol. I, pp. 7.1-7.24.
6. Foch, R. J., and Wyatt, R. E. (1986) "Low Altitude/Airspeed Unmanned Research Aircraft (LAURA) Preliminary Development," Proc. of the Conf. on Aerodynamics at Low Reynolds Numbers, Royal Aeronautical Society, London, Britain, October, Vol. III, pp. 31.1-31.29.
7. Hill, M. L. (1982) "Designing a MiniRPV for a World Endurance Record," Astro. & Aero., November, pp. 47-54.
8. Liu, H.-T. (1986) "Effects of Atmospheric Turbulence and Gust On the Performance of a Wortmann FX-63-137 Wing," Proc. of the Conf. on Aerodynamics at Low Reynolds Numbers, Royal Aeronautical Society, London, Britain, October, Vol. I, pp. 9.1-9.25.
9. McCroskey, W. J. (1982) "Unsteady Airfoils," Ann. Rev. Fluid Mech., Vol. 14, pp. 285-311.
10. McCroskey, W. J. (1981) "The Phenomena of Dynamic Stall," NASA Technical Memorandum 81264, Ames Research Center, Moffet Field, California, March, 28 pp.
11. Maresca, C., Favier, D., and Rebont, J. (1979) "Unsteady Aerodynamics of an Airfoil at High Angle of Incidence Performing Various Linear Oscillations in a Uniform Stream," Paper No. 12, Fifth European Rotorcraft and Powered Lift Aircraft Forum, Amsterdam, Netherlands.
12. Carta, F. O. (1979) "A Comparison of the Pitching and Plunging Response of an Oscillating Airfoil," NASA CR 3172, October, 153 pp.
13. Chen, S.-H. (1985) "The Unsteady Aerodynamics of Plunging Airfoil," Ph.D. Dissertation, Aerospace Engineering, University of Southern California, Los Angeles, May, 146 pp.

14. St. Hilaire, A. O., Carta, F. O., and Jepson, W. D. (1979) "The Influence of Sweep on the Aerodynamic Loading of an Oscillating NACA 0012 Airfoil," AHS Preprint 79-4.
15. Liiva, J. (1969) "Unsteady Aerodynamics and Stall Effects on Helicopter Rotor Blade Sections," J. Aircraft, Vol. 6, No. 1, pp. 46-51.
16. Liu, H.-T., Geller, E. W., and Cooper, M. (1985) "An Environmental Aerodynamic Test System for Low-Reynolds-Number Applications," Proc. Conf. on Low Reynolds Number Airfoil Aerodynamics, University of Notre Dame, Notre Dame, Indiana, June, pp. 207-218.
17. Bastedo, W. G., Jr., and Mueller T. J. (1985) "Performance of Finite Wings at Low Reynolds Number," Proc. Conf. on Low Reynolds Number Airfoil Aerodynamics, University of Notre Dame, Notre Dame, Indiana, June, pp. 195-205.
18. Marchman, J. F. III, Sumantran, V., and Schaefer, C. G. (1986) "Acoustic and Turbulence Influence on Stall Hysteresis," AIAA Paper No. 86-0170.
19. Pregler, W., Guignard, T., and Giles, M. (1981) "Aerodynamic Test System," Hang Gliding, March.
20. Marchman, J. F. III (1986) "Aerodynamic Testing at Low Reynolds Numbers," AIAA Paper 86-0179, New York, March.
21. Marchman, J. F. III, Abtahi, A. A., and Sumantran, V. (1985) "Aspect Ratio Effects on the Aerodynamics of Wortmann Airfoil at Low Reynolds Number," Proc. Conf. on Low Reynolds Number Airfoil Aerodynamics, University of Notre Dame, Notre Dame, Indiana, June, pp. 183-193.
22. Bendat, J. S., and Piersol, A. G. (1971) Random Data: Analysis and Measurement Procedures, Wiley-Interscience, New York.

END  
DATE  
FILMED

4-88  
DTIC